



HAL
open science

Mg²⁺-dependent conformational equilibria in CorA: an integrated view on transport regulation

Nicolai Tidemand Johansen, Marta Bonaccorsi, Tone Bengtsen, Andreas Haahr Larsen, Frederik Grøn-bæk Tidemand, Martin Cramer Pedersen, Pie Huda, Jens Berndtsson, Tamim Darwish, Nageshwar Rao Yepuri, et al.

► To cite this version:

Nicolai Tidemand Johansen, Marta Bonaccorsi, Tone Bengtsen, Andreas Haahr Larsen, Frederik Grøn-bæk Tidemand, et al. Mg²⁺-dependent conformational equilibria in CorA: an integrated view on transport regulation. 2021. hal-03853045v1

HAL Id: hal-03853045

<https://hal.science/hal-03853045v1>

Preprint submitted on 29 Nov 2021 (v1), last revised 15 Nov 2022 (v2)

HAL is a multi-disciplinary open access archive for the deposit and dissemination of scientific research documents, whether they are published or not. The documents may come from teaching and research institutions in France or abroad, or from public or private research centers.

L'archive ouverte pluridisciplinaire **HAL**, est destinée au dépôt et à la diffusion de documents scientifiques de niveau recherche, publiés ou non, émanant des établissements d'enseignement et de recherche français ou étrangers, des laboratoires publics ou privés.

1 Mg²⁺-dependent conformational equilibria in CorA: an 2 integrated view on transport regulation

3 Nicolai Tidemand Johansen^{*,1}, Marta Bonaccorsi^{*,2}, Tone Bengtsen^{*,3,4}, Andreas Haahr
4 Larsen^{1,4}, Frederik Grønbaek Tidemand¹, Martin Cramer Pedersen¹, Pie Huda⁵, Jens
5 Berndtsson⁶, Tamim Darwish⁷, Nageshwar Rao Yepuri⁷, Anne Martel⁸, Thomas Günther
6 Pomorski^{9,10}, Andrea Bertarello², Mark Sansom⁴, Mikaela Rapp⁶, Ramon Crehuet³, Tobias
7 Schubeis^{#,2}, Kresten Lindorff-Larsen^{#,3}, Guido Pintacuda^{#,2}, and Lise Arleth^{#,1}

8
9 *Equally contributing authors

10 #Corresponding author

11 Emails: tobias.schubeis@ens-lyon.fr, lindorff@bio.ku.dk, guido.pintacuda@ens-lyon.fr,
12 arleth@nbi.ku.dk

13
14 1 Condensed Matter Physics, Niels Bohr Institute, University of Copenhagen, Copenhagen,
15 Denmark

16 2 Centre de RMN à Très hauts Champs de Lyon (UMR 5280, CNRS / Ecole Normale
17 Supérieure de Lyon / Université Claude Bernard Lyon 1), University of Lyon, Villeurbanne,
18 France

19 3 Structural Biology and NMR Laboratory and Linderstrøm-Lang Centre for Protein Science,
20 Department of Biology, University of Copenhagen, Denmark

21 4 Department of Biochemistry, University of Oxford, Oxford, United Kingdom

22 5 Australian Institute for Bioengineering and Nanotechnology, The University of Queensland,
23 Brisbane, Australia

24 6 Department of Biochemistry and Biophysics, Center for Biomembrane Research,
25 Stockholm University, Stockholm, Sweden

26 7 National Deuteration Facility, Australian Nuclear Science and Technology Organization,
27 Lucas Heights, Australia

28 8 Institut Laue–Langevin, Grenoble, France

29 9 Section for Transport Biology, Department of Plant and Environmental Sciences,
30 University of Copenhagen, Frederiksberg, Denmark

31 10 Department of Biochemistry II – Molecular Biochemistry, Ruhr University Bochum,
32 Bochum, Germany

33

34

35 Abstract

36 The CorA family of proteins regulates the homeostasis of divalent metal ions in many bacteria,
37 archaea, and eukaryotic mitochondria, making it an important target in the investigation of the
38 mechanisms of transport and its functional regulation. Although numerous structures of open
39 and closed channels are now available for the CorA family, the mechanism of the transport
40 regulation remains elusive. Here, we investigated the conformational distribution and
41 associated dynamic behaviour of the pentameric Mg^{2+} channel CorA at room temperature
42 using small-angle neutron scattering (SANS) in combination with molecular dynamics (MD)
43 simulations and solid-state nuclear magnetic resonance spectroscopy (NMR). We find that
44 neither the Mg^{2+} -bound closed structure nor the Mg^{2+} -free open forms are sufficient to explain
45 the average conformation of CorA. Our data support the presence of conformational equilibria
46 between multiple states, and we further find a variation in the behaviour of the backbone
47 dynamics with and without Mg^{2+} . We propose that CorA must be in a dynamic equilibrium
48 between different non-conducting states, both symmetric and asymmetric, regardless of
49 bound Mg^{2+} but that conducting states become more populated in Mg^{2+} -free conditions. These
50 properties are regulated by backbone dynamics and are key to understanding the functional
51 regulation of CorA.

52 Introduction

53 Magnesium is the most abundant divalent cation (Mg^{2+}) inside the cell, where it is mainly
54 associated with the biological energy source adenosine triphosphate and other negatively
55 charged molecules¹. Mg^{2+} serves several biological functions, e.g. as co-factor for enzymes¹,
56 and Mg^{2+} deficiency is linked to severe diseases including cardiac syndromes, muscular
57 dysfunction and bone wasting²⁻⁴. CorA is the main ion channel for Mg^{2+} -import in most bacteria
58 and archaea⁵. Despite little sequence conservation, CorA shares two membrane spanning
59 helices and a conserved GMN motif with eukaryotic homologs, including Mrs2 that is
60 responsible for Mg^{2+} -import to the mitochondrial lumen and is essential for cell survival^{6,7}.

61 Several structures determined by X-ray crystallography are available for *Thermotoga maritima*
62 CorA (TmCorA)⁸⁻¹². All wild-type proteins have been crystalized as nearly symmetric
63 pentamers in the presence of divalent metal ions and all represent a non-conducting state of
64 the channel with a narrow and hydrophobic pore. **Figure 1A** shows a representative structure,
65 which is characterized by a transmembrane domain (TMD) connected to the intracellular
66 domain (ICD) by a long stalk helix. The periplasmic entrance to the pore contains the

67 conserved GMN motif that presumably binds to Mg^{2+} via its first hydration shell and thereby
68 acts as a selectivity filter^{11,13,14}. The ICD contains ten inter-protomer binding sites for Mg^{2+} (two
69 per protomer, denoted M1 and M2) involved in regulating the channel^{11,15,16}. The open state(s)
70 of CorA have so far not been crystallized, but several biochemical and structural studies^{15,16}
71 as well as molecular dynamics simulations¹² have pinpointed the determining residues
72 involved in gating and suggested open models. One model suggests pore dilation upon loss
73 of Mg^{2+} at the M1 (and M2) sites due to a concerted iris-like movement^{16,17}, while another
74 suggests a hydrophobic-to-polar transition of the pore upon concerted rotation of the stalk
75 helices^{18,19}.

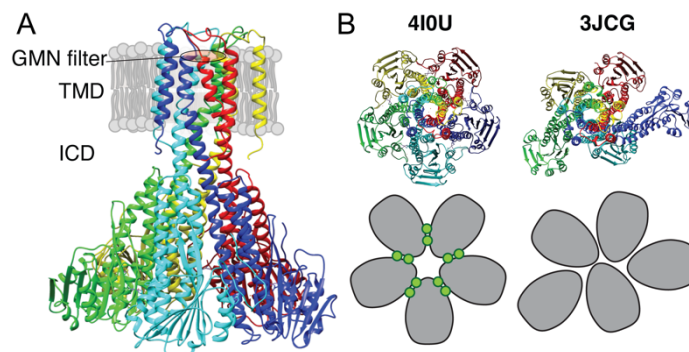
76

77 Recently, cryo-EM structures were obtained both in the presence and absence of Mg^{2+} ²⁰. The
78 Mg^{2+} bound structure at ~ 3.8 Å resolution was symmetric and closed, in line with crystal
79 structures, whereas two Mg^{2+} -free structures at ~ 7.1 Å were symmetry broken and with dilated
80 pores. **Figure 1B** shows an intracellular view of the symmetric and asymmetric states,
81 highlighting the symmetry break upon removing Mg^{2+} . From these observations, the proposed
82 model involves a sequential destabilisation of CorA upon Mg^{2+} removal, leading to a highly
83 dynamic protein with shuffling protomers in the ICD, increasing the likelihood of pore dilation
84 and wetting events^{20,21}. Recent coarse grained MD simulations revealed the residue level
85 details of how a complex interaction network involving asymmetric movements of ICD
86 monomers ultimately leads to a conducting state upon removal of Mg^{2+} ²². High-speed atomic
87 force microscopy (HS-AFM) data on densely packed CorA in lipid bilayers supported this
88 model, but at the same time provided more insight to the dynamic interconversion of different
89 states, including a fourth population of highly asymmetric CorA, not resolved by cryo-EM²³.
90 Interestingly, this population accounted for most observed conformations at low Mg^{2+}
91 concentrations, supporting that CorA is a dynamic protein with a relatively flat energy
92 landscape and, potentially, multiple open states. However, CorA mutants with mutated
93 regulatory M1 sites were still able to crystallize in the (symmetric) closed state¹⁹, suggesting
94 that inter-protomer binding of Mg^{2+} is not required for closing the channel. Overall, the cryo-
95 EM and AFM experiments hint towards a highly dynamic ensemble of primarily asymmetric
96 states at low Mg^{2+} concentrations, while the successful crystallisation of M1 site mutants
97 suggests that the closed state is significantly present at these conditions.

98

99 In this study, we investigated CorA using two room-temperature methods, namely small-angle
100 neutron scattering (SANS), sensitive to large amplitude conformational changes and magic-
101 angle spinning solid-state NMR (MAS NMR), sensitive to structure and dynamics with atomic
102 resolution^{24,25}. For both methods, we employ custom developed state-of-the-art methodology,

103 i.e. size-exclusion chromatography (SEC) coupled to SANS^{26,27} and match-out deuterated
104 carrier systems for SANS^{28,29} (so-called stealth carrier systems), and >100 kHz MAS NMR in
105 lipid bilayers^{30,31}. Based on these data in conjunction with molecular simulations and
106 modelling, we propose a model in which CorA is in a dynamic equilibrium between symmetric
107 and asymmetric states, independent of bound Mg²⁺, but where an ensemble of conducting
108 states is energetically more favourable for Mg²⁺-free CorA due to increased conformational
109 dynamics resulting from the released electrostatic constraint.
110



111
112 **Figure 1** X-ray and cryo-EM structures of CorA. A: Side view of symmetric CorA (PDB ID:
113 4I0U) in presence of Mg²⁺ (“closed form”). B: Top view of the same symmetric state of CorA
114 (PDB ID: 4I0U) side-by-side to one of the asymmetric states observed in the absence of Mg²⁺
115 (“open form”) (PDB ID: 3JCG). A schematic representation of the two forms is shown below
116 their structures, with each monomer shown in gray and Mg²⁺ ions represented as green circles.

117 Results

118 CorA is structurally similar in presence and absence of Mg²⁺

119 The published cryo-EM structures of CorA in absence of Mg²⁺ (**Figure 1B**, 3JCG) reveal large
120 structural rearrangements compared to the nearly symmetric, non-conductive state obtained
121 from crystallography (**Figure 1B**, 4I0U). SANS curves calculated from these two structural
122 states of CorA reveal a significant change in the scattering curve in the region $q = 0.08 \text{ \AA}^{-1} -$
123 0.15 \AA^{-1} (**Figure 2A** and **Figure 2B**, right panels), i.e. on a length scale that is well-covered in
124 a standard SANS experiment. To match the cryo-EM conditions, we performed SANS
125 measurements in n-dodecyl-B-D-maltoside (DDM) detergent micelles and 2-Oleoyl-1-
126 palmitoyl-sn-glycero-3-phosphocholine (POPC) lipid nanodiscs. We used selectively
127 deuterated versions of both carrier types that were homogeneously matched-out and hence
128 invisible at 100 % D₂O; i.e. stealth DDM (sDDM) and stealth nanodiscs (sND, Figure 2-figure
129 supplement 1). Strikingly, the measured SANS curves are pair-wise indistinguishable in the
130 absence of Mg²⁺ (1 mM EDTA) and in the presence of 40 mM Mg²⁺ for the sDDM (**Figure 2A**)
131 and sND (**Figure 2B**) samples, respectively, indicating no significant difference in the average
132 conformations of the Mg²⁺-free and bound states of CorA. This observation contrasts with the

133 recently proposed large-scale structural rearrangements reported from cryo-EM and high-
134 speed AFM data.

135

136 We note that the SANS data obtained on the sND samples (**Figure 2B**) have a slight excess
137 scattering contribution at low- q compared to the sDDM samples (**Figure 2A**), which can be
138 attributed to the presence of a few *E. coli* endogenous lipids in the sND samples. However,
139 the SANS data from sDDM and sND samples are indistinguishable in the q -region expected
140 to reveal differences from symmetric and asymmetric states (Figure 2-figure supplement 2),
141 which confirms that CorA exhibits the same behaviour in a POPC lipid environment and in
142 DDM detergent carriers. The rightmost panels of **Figure 2A** and **Figure 2B** show enhanced
143 views on this region for the SANS data compared to the SANS curves calculated from the
144 PDB structures. Interestingly, neither of the curves calculated from the PDB structures match
145 the measured SANS data, suggesting that the solution structure of CorA cannot be described
146 by any of these single structures, regardless of whether or not CorA is in the presence of Mg^{2+} .

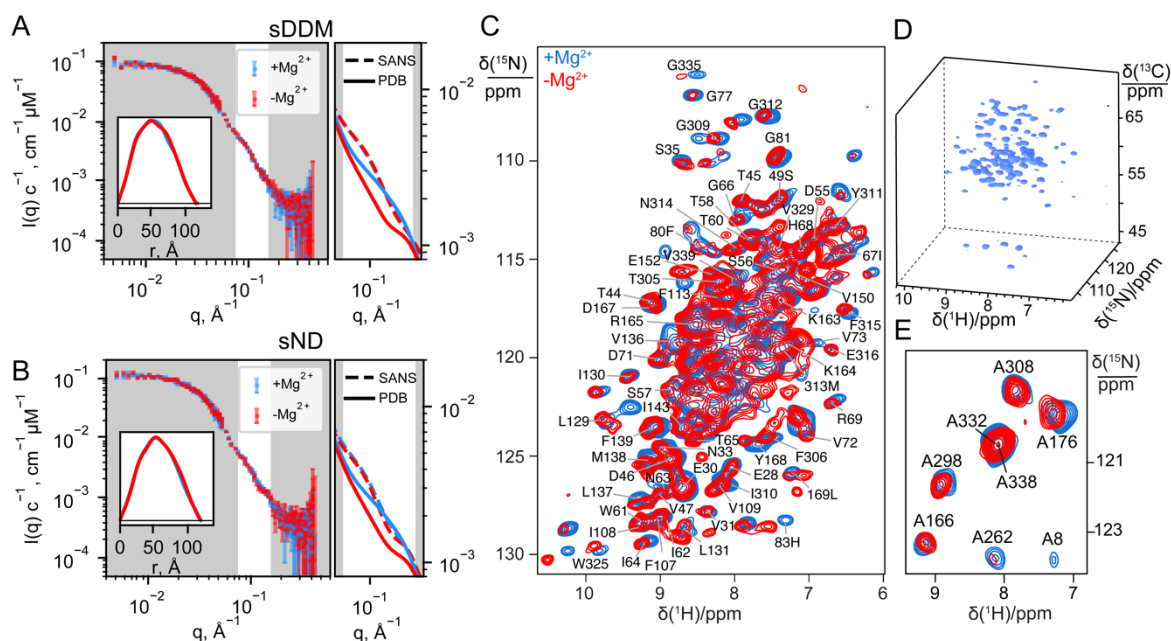
147

148 While SANS data provided information on the overall molecular shape of CorA in the two
149 preparations, we used MAS NMR to obtain insight into structural changes at the residue-level
150 length-scale. MAS NMR data were recorded on uniformly ^{13}C , ^{15}N -labelled CorA, reconstituted
151 in 1,2-dimyristoyl-sn-glycero-3-phosphocholine (DMPC) lipid bilayers, in the presence or
152 absence of Mg^{2+} . Backbone resonance assignment was obtained at high Mg^{2+} concentration
153 acquiring a set of three-dimensional experiments relying on $^1H^N$ and 1Ha detection with 100
154 kHz MAS. We were able to annotate ~ 100 peaks to residues spread throughout the structure
155 of CorA. Notably, the assignment of CorA with and without Mg^{2+} is clustered in the globular
156 region in the ICD and in the TMD, including the important periplasmic loop, whereas only
157 sparse assignments were established in the long portion (243-289) of the stalk helix
158 connecting the two regions. The determination of random coil chemical shift deviation (CSD)
159 values confirmed that the secondary structure is in good agreement with the one obtained by
160 X-ray crystallography and Cryo-EM.

161

162 2D 1H - ^{15}N dipolar correlation spectra represent direct structural “fingerprints” of CorA in the
163 two preparations. Despite the high signal overlap associated to the high molecular weight of
164 CorA, fast MAS rates and the ultra-high magnetic field guarantee high sensitivity and feature
165 numerous signals with a resolution sufficient to track subtle structural changes. Once again,
166 against our expectations, we remarked that the spectra with and without Mg^{2+} showed very
167 little difference, with the positions of the resolved peaks differing less than 0.1 ppm in the two
168 forms and without peak splitting or broadening that would indicate distinct conformations
169 (**Figure 2C**).

170 Two parallel strategies were pursued to extend the analysis to the more crowded regions.
 171 First, we acquired three-dimensional (3D) experiments which correlate the amide proton and
 172 nitrogen with the C_α-carbon within each residue and thus include an additional ¹³C chemical
 173 shift dimension (**Figure 2D**). The resulting 3D spectra confirmed negligible chemical shift
 174 variations over more than ~90 sites across the TMD and ICD. In the Mg²⁺-free sample,
 175 however, a notable decrease in signal intensity was observed for most residues, resulting in
 176 the complete disappearance of two thirds of the peaks from the TMD (vide infra).
 177 Secondly, we used amino acid-specific isotopic enrichment to select the NMR signals
 178 associated to the amide groups of the alanine residues. Each CorA protomer contains eight
 179 alanine residues, distributed with four in the TMD and four in the ICD, which were all visible
 180 and assigned in the corresponding ¹H-¹⁵N dipolar correlation spectra of two preparations with
 181 and without magnesium (**Figure 2E**). Also, in this case, the spectra are superimposable and
 182 show no evidence of peak splitting.
 183 In conclusion, and in line with SANS, the NMR data show that the predominant structure of
 184 CorA in lipid bilayers is unaltered by the removal of Mg²⁺.
 185



186
 187 **Figure 2** Experimental data on CorA in presence (blue) and absence (red) of Mg²⁺. A+B:
 188 Experimental SANS data of CorA embedded in stealth DDM micelles (sDDM) and stealth
 189 nanodiscs (sND), respectively, with $p(r)$ -distributions calculated on BayesApp³² in the inset.
 190 The rightmost plots show zoomed comparisons of the $p(r)$ -fits of experimental data (SANS,
 191 dashed lines) with the SANS curves calculated on the X-ray (4I0U) and cryo-EM (3JCG)
 192 structures (PDB, full lines). Complete fits based on the PDB structures are shown in Figure
 193 4A. C: 2D ¹H-¹⁵N dipolar correlation spectra by MAS NMR of CorA embedded in hydrated
 194 DMPC bilayers recorded at 1 GHz ¹H Larmor frequency and 107 kHz MAS. D: Cube
 195 representation of a 3D ¹H-¹⁵N-¹³C spectrum. E: 2D ¹H-¹⁵N dipolar correlation spectra
 196 obtained for ¹⁵N-Alanine labeled CorA recorded at 1 GHz ¹H Larmor frequency and 60 kHz
 197 MAS. In C and E, site-specific assignments are annotated for resolved resonances.

198 **Figure 2-figure supplement 1** Validation of nanodisc match-out deuteration. A: Background
199 subtracted SANS data measured on sNDs in different percentage of D₂O. B: Comparison of
200 unsubtractd SANS data and corresponding background measurement in 100 % D₂O. C: Plot
201 of contrast vs D₂O to verify match-point of sample (fitted to 99.9 % D₂O by linear regression).
202 I(0) values were determined using Guinier fits to the low-q data (grey points) as highlighted in
203 the insert. The Guinier fit to the SANS data at 100 % D₂O has not been shown due to the large
204 errorbars, and the fit was also not included for fitting the contrast vs D₂O. D: SAXS data on
205 sND collected in H₂O buffer together with p(r) distribution (insert). A nanodisc model³³ was
206 fitted to the data using WillItFit³⁴, producing a great fit, as evaluated by the residual plot on the
207 bottom.

208 **Figure 2-figure supplement 2** Comparison of SANS data in sDDM and sND. Same data as
209 shown in Figure 1D-E, but presented here to compare data collected in sDDM vs sND. Despite
210 the slightly higher forward scattering in the sND data, the SANS data from the two different
211 systems overlap in the region of interest, as highlighted. Given that CorA had spent less time
212 and steps in presence of DDM prior to reconstitution in sNDs, the excess signal likely stems
213 from a small number of tightly bound E. coli lipids that do not match out in D₂O. By comparing
214 the extrapolated values of I(0) between the sDDM and sND samples, we estimated the number
215 to be on the order of 10 lipids, i.e. two lipids per protomer. Although the presence of visible
216 lipids would complicate further detailed analysis, the striking identity of the measured
217 curves with and without Mg²⁺ in sNDs supports no large structural rearrangements.

218

219

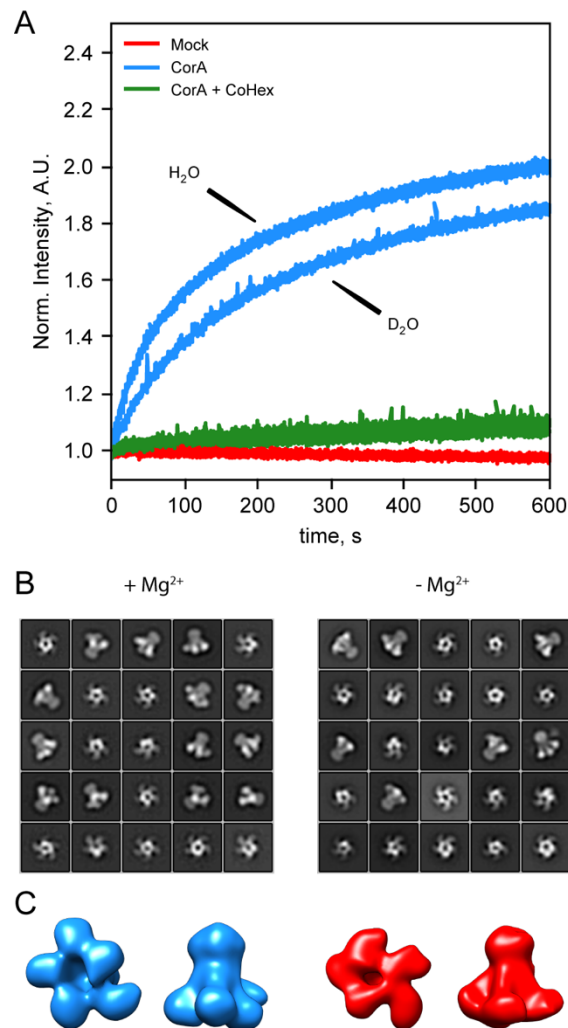
220 **CorA is active and preserves its tertiary structure in D₂O**

221 Since Mg²⁺ hydration plays an important role in CorA selectivity, and D₂O and H₂O have
222 slightly different physicochemical properties³⁵, we speculated whether the identical SANS
223 curves with and without Mg²⁺ were due to CorA losing its activity in the SANS condition, i.e. at
224 100% D₂O. To test this, we measured the activity of CorA in POPC liposomes under the SANS
225 conditions by a fluorometric assay (**Figure 3A**). This analysis shows that CorA is clearly active
226 in D₂O. The transport rate estimated from the initial linear part of the trace is lower by less
227 than a factor of two compared to H₂O. A slightly reduced rate in D₂O has been reported for
228 other membrane proteins³⁶ and is explainable by slightly altered properties of the two
229 solvents^{35,37}. We could also inhibit CorA activity in D₂O with Co[NH₃]₆³⁺ (**Figure 3A**, green),
230 supporting that the protein is indeed functional under the SANS conditions.

231

232 We further carried out negative stain EM on samples of CorA in DDM and D₂O with or without
233 Mg²⁺. The refined 2D classes clearly show that the pentameric architecture of CorA is
234 preserved in D₂O in both conditions (**Figure 3B**). Furthermore, several 2D classes appear to
235 exhibit approximate fivefold symmetry, both in the presence and absence of Mg²⁺. To avoid
236 bias, we refined 3D models without imposing symmetry (**Figure 3C**). In both conditions, these
237 low-resolution 3D models (~ 15 Å) are reminiscent of the overall expected architecture of CorA
238 (**Figure 1**), but notably show some degree of asymmetry. In conclusion, CorA show little to no
239 perturbation from measurements in D₂O, rendering the SANS data sets viable for modelling
240 of the solution structure of CorA.

241



242

243 **Figure 3** CorA activity in D₂O and direct visualization by negative stain EM. A: CorA activity in
 244 the conditions used for SANS. The traces are the normalized fluorescence signals after adding
 245 Mg²⁺ to either empty POPC liposomes (Mock), CorA-POPC proteoliposomes (CorA), or CorA-
 246 POPC proteoliposomes preincubated with the inhibitor Co[NH₃]³⁺ in D₂O (CorA + CoHex). B:
 247 Negative stain EM of CorA in DDM and D₂O with and without Mg²⁺. The 25 most abundant 2D
 248 classes are shown for each condition. The box dimensions are 170 x 170 Å² for scale. C: Final
 249 3D model for each condition shown from the intracellular side and in side-view, respectively.

250

251 Model refinement to SANS data shows that CorA is asymmetric

252 The SANS data sets obtained in sDDM (**Figure 2A**) exhibit well-defined Guinier-regions and
 253 the calculated radii of gyration, R_g, of 42.1 ± 1.3 Å (+ Mg²⁺) and 43.8 ± 1.7 Å (- Mg²⁺) are close
 254 to the predicted values from the X-ray (41.3 Å) and cryo-EM structures (42.2 Å and 42.3 Å).
 255 Thus, these data are indicative of well-separated CorA pentamers with no interference from
 256 visible lipids or the kind, providing the optimal basis for structural modelling. Given the
 257 identity of the SANS data obtained on the samples of CorA in sDDM with and without Mg²⁺,
 258 we performed structural modeling on only a single data set, that is CorA in sDDM without Mg²⁺
 259 (**Figure 2A**, red). Despite controversies on the open state, there is consensus that the

260 crystallized symmetric state represents the closed state of the protein. Surprisingly, we could
261 not obtain good fits of the symmetric state to our SANS data without clear systematic
262 deviations, especially at the feature present at $q \approx 0.1 \text{ \AA}^{-1}$ (**Figure 4A**, 4I0U). This was also
263 the case for the asymmetric cryo-EM structure (Figure 4A, 3JCG) that produced an even
264 worse fit. In SANS, the signal represents a population-weighted average of all conformations
265 that the protein can adopt. With a measurement time on the order of several minutes and
266 illumination of $\approx 10^{12}$ - 10^{13} molecules, all accessible populations are expected to contribute to
267 the signal. A relatively flat energy landscape with multiple interconverting states has been
268 proposed in Mg^{2+} -free conditions, making a fit of a single structure less meaningful in this
269 context. However, it is unlikely that the average of an ensemble of asymmetric structures give
270 rise to the same SANS signal as that of a single symmetric state corresponding to the structure
271 determined by crystallography and cryo-EM in high Mg^{2+} .

272

273 With no scattering contribution from the carrier systems, it becomes possible to analyse the
274 SANS data by conventional methods for soluble proteins, such as bead-modeling. When
275 imposing P5 symmetry, we could obtain envelopes reminiscent of the CorA structure by bead-
276 modelling (Figure 4-figure supplement 1B), whereas no symmetry (P1) imposed lead to
277 asymmetric mass distributions that were not at all compatible with the overall architecture of
278 CorA (Figure 4-figure supplement 1A). This indicates that there is significant structural
279 dispersion in the sample.

280

281 To obtain a molecular constrained model compatible with the data, we applied a modified type
282 of normal mode analysis (NMA), starting from the closed crystal structure. A structure with
283 mostly intact secondary structure but a high degree of asymmetry in the ICDs yielded a great
284 fit to the SANS data (**Figure 4B**). Importantly, this model describes the feature at $q \approx 0.1 \text{ \AA}^{-1}$,
285 where the PDB models deviate the most. Thus, on average, the solution structure of CorA
286 appears to be asymmetric, in line with our EM models (**Figure 3C**). Again, we emphasize that
287 such an overall asymmetric structure of CorA in presence of excess Mg^{2+} is in stark contrast
288 to the picture of a closed, symmetric structure that has served the basis for all proposed
289 mechanisms of Mg^{2+} gating. However, a single asymmetric model as derived from NMA
290 (**Figure 4B**) is neither compatible with a single set of peaks in NMR (**Figure 2C** and **Figure**
291 **2E**) nor the substantial experimental evidence for a nearly symmetric, closed state in presence
292 of Mg^{2+} . Likely, CorA adopts multiple different states^{20,23}, and according to our data does so
293 both with and without Mg^{2+} bound. In this case, the SANS data would represent the number
294 weighted average of different states that must be overall asymmetric.

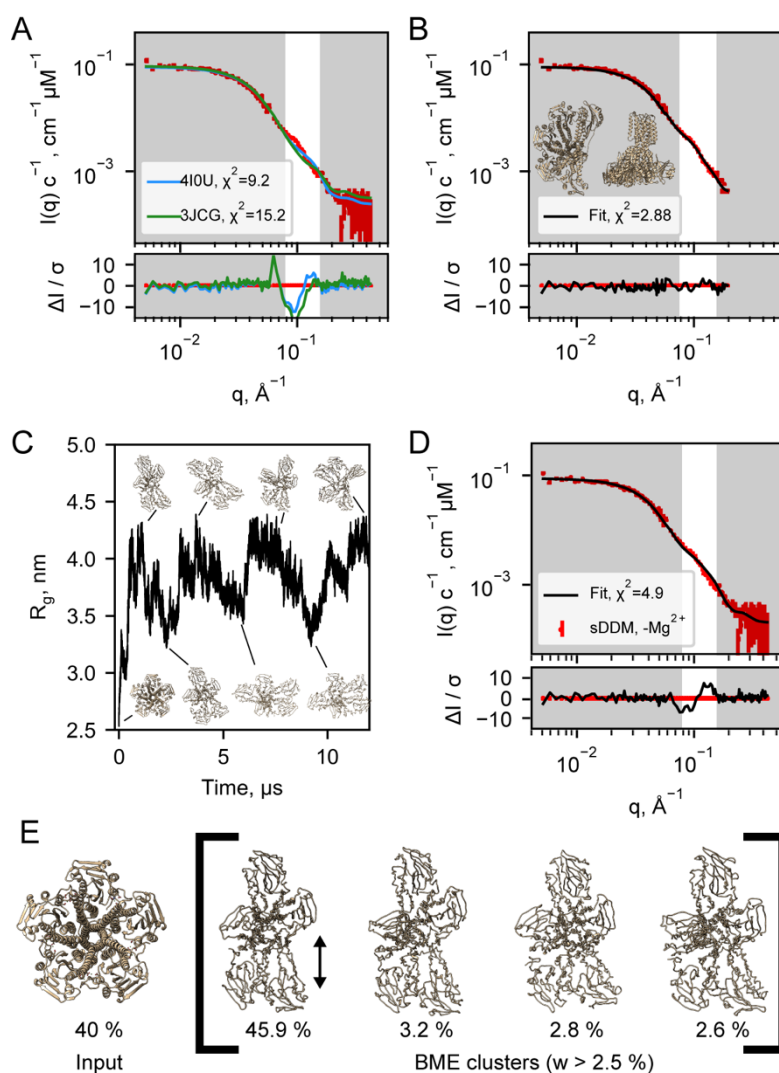
295

296 To model the apparent asymmetry in CorA in more detail, we performed coarse grained
297 molecular dynamics simulations (MD). First, we set up CorA embedded in a POPC bilayer
298 using the Martini3.0b force field. Starting from the symmetric or asymmetric structures, 32 μs
299 and 20 μs simulations, respectively, without any inter-chain elastic network terms yielded only
300 small structural fluctuations (data not shown), which did not significantly improve fits to the
301 experimental SANS data, especially not around the feature at $q \approx 0.1 \text{ \AA}^{-1}$. Thus, we extended
302 the analysis to metadynamics simulations (MetaD) that allows for enhanced sampling of
303 structural dynamics. MetaD drives the simulation towards a larger variety of structural states
304 based on an energetic bias on a structural feature, a so-called collective variable, here the R_g
305 on specific ICD residues. Starting from the symmetric structure, the MetaD simulation quickly
306 drove the simulation away from the local structural minimum that the standard MD had been
307 trapped in and sampled a large range of conformationally different structures (**Figure 4C**).

308
309 The averaged back-calculated SANS of the entire ensemble of structures obtained from
310 MetaD simulations did not fit the experimental SANS data satisfactorily (data not shown). This
311 can be explained by inaccuracies in the simulation that arise from e.g. inaccuracies in the
312 coarse grained force field and imprecisions in the simulation that in turn arise from e.g.
313 insufficient sampling. To resolve this, we applied the Bayesian/Maximum Entropy reweighting
314 method (BME) to optimize the weights of the individual conformations in the simulation with
315 the aim of obtaining an ensemble in better agreement with the experimental SANS data. In
316 addition to the BME, we enforced that a symmetric state should be present in the final
317 ensemble, given the substantial experimental evidence for this state in the literature and that
318 it was under-sampled in the simulation. The best fit to the SANS data (**Figure 4D**) was
319 obtained with an ensemble consisting of $40\% \pm 28\%$ symmetric CorA and the remainder of
320 asymmetric conformations from the MetaD (**Figure 4E** and Figure 4-figure supplement 3).
321 Despite some systematic deviations, the fit is much improved with regards to describing the
322 feature in the SANS data at $q \approx 0.1 \text{ \AA}^{-1}$, as compared to the fits obtained with the symmetric
323 crystal structure or the open cryo-EM structures, respectively (**Figure 4A**).

324
325 To visualise the results of the MetaD simulation and hence the simulated dynamics, we cluster
326 similar structures and show the four most predominant cluster centroids (**Figure 4E**) where
327 especially one cluster predominate in the final fitted ensemble. Although the four cluster
328 centroids are wide apart in simulation time ($\approx 500 \text{ ns}$), they are structurally similar with a
329 maximum pairwise RMSD of 6.5 \AA (data not shown). The main difference is the distance
330 between the two protomers (**Figure 4E**, black arrow), which indicate that the individual
331 domains of the ICD can move relative to each other. This is in line with the subunit

332 displacements described in the symmetry-break based gating model derived from the cryo-
 333 EM structures and supported by AFM measurements. Importantly, however, we find that these
 334 movements occur irrespective of the presence of Mg^{2+} . Interestingly, CorA mutants were
 335 recently shown to crystallize in the symmetric, closed state without Mg^{2+} bound at the
 336 regulatory M1 sites. While the channel is surely closed in the presence of high Mg^{2+} , this
 337 observation challenges the claim that release of interfacial bound Mg^{2+} is the cause for
 338 symmetry-break and opening of the channel at low Mg^{2+} levels. In light of this, our data suggest
 339 that CorA could also be in an asymmetric, closed state at high Mg^{2+} levels. Indeed, we find
 340 that the structure of CorA is better described as a distribution of symmetric and asymmetric
 341 structures with no large-scale conformational differences between the open and closed states.
 342



343
 344 **Figure 4** Structural modeling of CorA from SANS data. A: Model fits of the closed crystal
 345 structure (410U) and open cryo-EM structure (3JCG) to the experimental SANS data obtained
 346 in sDDM without Mg^{2+} . The bottom panel shows the error-normalised difference plot of the fits.
 347 B: Model fit of the structure obtained by regularised normal mode analysis (bottom and side
 348 views inserted on plot). C: MetaD molecular dynamics trajectory with representative frames
 349 visualized as ribbon structures. D: Fit of a weighted ensemble obtained from the MD simulation

350 *in B together with a 40 % contribution from the symmetric CorA. E: The 4 highest weighted*
351 *cluster centroids in the metaD simulation (right bracket) together with the closed symmetric*
352 *structure (left) which together illustrates the ensemble of CorA structures that produced the*
353 *best fit to the experimental SANS data.*

354 **Figure 4-figure supplement 1** *Bead modeling of CorA. All four SANS data sets were*
355 *analysed by the DAMMIF pipeline³⁸ available from the ATSAS package³⁹. In total, DAMMIF*
356 *was run 100 times in slow mode with either P1 (A) or P5 (B) symmetry selected. For P1*
357 *symmetry, the normalized spatial discrepancy (NSD) values varied from 1.2 to 1.5, whereas*
358 *for P5 symmetry, NSD values varied from 1.4 to 1.7. NSD values above 1 indicate that the*
359 *calculated models differ systematically from one another.*

360 **Figure 4-figure supplement 2** *Goodness of fit from NMA generated structures to SANS. The*
361 *best compromise between conservation of structure and the best fit to the data is in the*
362 *“elbow”-region, here chosen at $S = 0.01$ (with $\alpha = 600$).*

363 **Figure 4-figure supplement 3** *Ensemble fitting to SANS data with symmetric CorA included.*
364 *The goodness of fit (χ^2) plotted as a function f , the fraction of 4IU, fixed before BME*
365 *reweighting of the MetaD generated ensemble to fit the SANS data. The data on the graph*
366 *were fitted by a quadratic function to yield the minimum with standard deviation at 40 ± 28 %*
367 *4IU, where the standard deviation was calculated by an increment in χ^2 of 1.*

368 **Structural dynamics are different in open and closed states of CorA**

369 So far, we have considered a set of static snapshots to interpret the wide variety of populated
370 states of CorA. The observation of MAS NMR dynamical probes sheds light on the backbone
371 motions of these states over different timescales, enriching the structural description of CorA
372 with conformational plasticity.

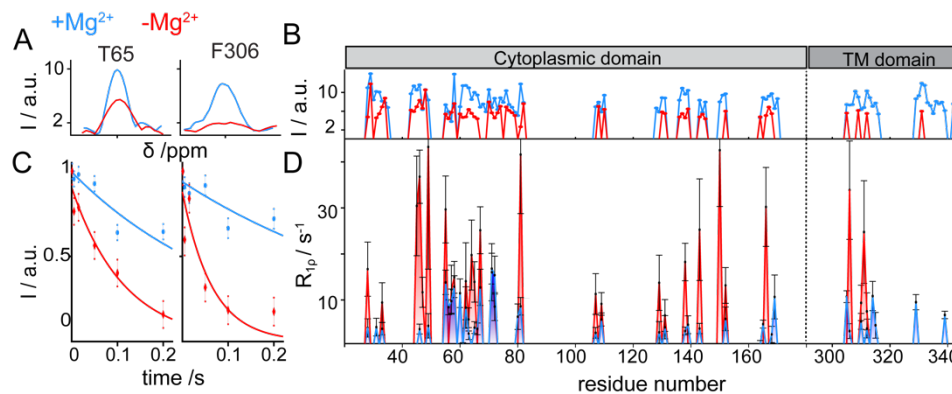
373 A first insight on site-specific dynamics is obtained by comparing the peak intensities observed
374 in the MAS NMR experiments in the two samples with and without Mg^{2+} .

375 Peak intensities are dependent on dipolar couplings between nearby nuclei and are affected
376 when such couplings are averaged by local motions. For an amide 1H - ^{15}N pair, this
377 corresponds to motional processes faster than \sim tens of kHz (i.e. more rapid than \sim hundreds
378 of μs).

379 Changes in peak intensity are already noticeable in the 2D 1H - ^{15}N dipolar correlation spectra,
380 but are amplified in the 3D correlations, where additional radio-frequency irradiation periods
381 act as a more stringent filter, dumping the signals of the most mobile sites. 1D traces of two
382 exemplar 3D 1H - ^{15}N - ^{13}C correlations (T65 in the ICD and F306 in the TMD) and the plot of
383 signal intensities over the full protein sequence with and without Mg^{2+} are shown in **Figure 5A**
384 and **Figure 5B**, respectively. As mentioned above, an overall decrease in peak intensities is
385 associated to removal of Mg^{2+} , with a stronger effect observed in the TMD. This points toward
386 a variation of the dynamic behavior of this region in the two samples.

387 ^{15}N spin-lattice relaxation rates in the presence of a spin-lock field ($^{15}N R_{1\rho}$) are sensitive
388 reporters of motions occurring over a window of hundreds of ns to hundreds of μs . These
389 parameters were measured site-specifically for ~ 40 residues in CorA backbone, by introducing

390 a relaxation filter in the ^1H - ^{15}N dipolar correlation module and monitoring the signal decay of
391 each amide pairs in a series of experiments with increasing relaxation delays (**Figure 5C**). A
392 remarkable (up to 10 fold) increase was observed throughout the entire protein upon removal
393 of Mg^{2+} (**Figure 5D**). The same effect was observed for the ^{15}N -alanine labelled sample (Figure
394 5-figure supplement 1A). An additional measurement of ^{15}N $R_{1\rho}$ rates upon a $\sim 20^\circ\text{C}$ cooling
395 revealed a different temperature-dependent behaviour of the two Mg^{2+} -loaded samples
396 (Figure 5-figure supplement 1B). While in the presence of Mg^{2+} relaxation rates were
397 conserved at low temperatures, an important (2-3 fold) decrease was observed in the Mg^{2+} -
398 free form. Finally, also dynamics on the ns timescale obtained by the measurements of bulk
399 backbone ^{15}N R_1 showed a global increase of relaxation rates (by a factor ~ 1.5) upon removal
400 of Mg^{2+} (Figure 5-figure supplement 1C).
401 In summary, MAS NMR reveals that removal of Mg^{2+} triggers an increase in the backbone
402 flexibility on different timescales, a dynamical effect which is different for the ICD and the TMD.



403

404 **Figure 5** CorA backbone dynamics by MAS NMR in DMPC in presence (blue) and in absence
405 (red) of Mg^{2+} . A: Examples of 1D traces of 3D ^1H - ^{15}N - ^{13}C peaks for two residues in the ICD
406 (T65) and in the TMD (F306). B: Comparison of peak intensities in 3D ^1H - ^{15}N - ^{13}C spectra over
407 the protein sequence. ICD and TMD are indicated by boxes of different color on top of the plot.
408 C-D: Site-specific ^{15}N $R_{1\rho}$ rates measured with a 15 kHz spin-lock field. C: Examples of ^{15}N
409 $R_{1\rho}$ relaxation decays together with the corresponding mono-exponential fits for residues T65
410 and F306. D: Comparison of site-specific backbone ^{15}N $R_{1\rho}$ rates plotted along the CorA
411 sequence.

412 **Figure 5-figure supplement 1** CorA backbone dynamics by MAS NMR: Site-specificity and
413 temperature dependence. A: Site-specific ^{15}N $R_{1\rho}$ rates measured with a 15 kHz spin-lock field
414 in the ^{15}N -Ala sample of CorA. B: Comparison of site-specific ^{15}N $R_{1\rho}$ rates measured with a
415 15 kHz spin-lock field at $\sim 280\text{ K}$ in the presence (cyan) and in the absence (magenta) of Mg^{2+} .
416 Dashed lines indicate the average relaxation rate values in the ICD and TMD distinctly, at
417 higher (blue and red) and lower (cyan and magenta) temperature. C: Bulk ^{15}N R_1 decay curves
418 measured at 300 K. Experimental curves were fitted with a biexponential decay.

419 Discussion

420 The functional mechanism of the pentameric divalent cation channel CorA of *Thermotoga*
421 *maritima* has been under investigation since the release of the first high resolution structures

422 in 2006. It is now well acknowledged that gating involves a conformational transition between
423 a closed symmetric state and one or many asymmetric states. The concise current model
424 derived from cryo-EM²⁰ and HS-AFM²³ defines a rigid symmetric conformation at high Mg²⁺
425 concentrations (>4 mM), dynamic asymmetric conformations at low Mg²⁺ concentrations (2-3
426 mM) and several distinct rigid asymmetric conformations in the absence of Mg²⁺.
427 We have performed SANS in invisible carrier systems to study the solution conformation of
428 CorA, together with modelling of both static and ensemble structures obtained from MetaD
429 simulations. Furthermore, we used ¹H-detected solid-state NMR to investigate CorA
430 conformation and dynamics in hydrated lipid bilayers. These complementary methods allow
431 us to expand the current view on the mechanistically important conformational equilibria.

432

433 **Asymmetric states are populated in CorA at high Mg²⁺ concentrations.** Crystal structures
434 of CorA from *Thermotoga maritima* (*Tm*) and *Methanocaldococcus jannaschii* (*Mj*) solved in
435 the Mg²⁺-bound state revealed a symmetric bell-like structure, showing a narrow inner
436 channel, representing the closed form. All proposed gating models were built on the common
437 basis of a single rigid and symmetric conformation at high Mg²⁺ concentrations^{11,12,16,20,23,40,41}.
438 Our SANS data recorded on CorA in high Mg²⁺ concentrations is inconsistent with a single
439 symmetric structure and can only be explained by symmetry breaking and/or a mixture of
440 populations e.g. through the concomitant presence of symmetric and asymmetric states.
441 Indirect indications for a mixture of populations even in the presence of Mg²⁺ can be found in
442 the literature: For example, the symmetric cryo-EM structure (3JCF) obtained at high Mg²⁺
443 concentrations, resulted from roughly 60% of the particles²⁰, which implies that asymmetric
444 states could partly account for the remaining 40%. Although with lower resolution, our
445 negative-stain TEM data indeed support the presence of such populations.

446 HS-AFM measurements²³ showed that the symmetric, closed state was stable in starting
447 conditions at high Mg²⁺. However, only 35 % of this state was recovered after complete
448 removal and reintroduction of Mg²⁺ ions, suggesting secondary effects working on adjusting
449 the equilibrium between fluctuating asymmetric states and the closed symmetric state.

450

451 **A symmetric state is populated in CorA in absence of Mg²⁺.** The conformation of metal-
452 free CorA has been the object of a long ongoing speculation since wild-type CorA failed to
453 crystallize in the absence of Mg²⁺. Asymmetric subunit arrangements were first proposed
454 based on an X-ray structure of a truncated CorA variant (Δ N25/R222A/K223A)¹². Since the
455 release of two cryo-EM structures of wild-type CorA²⁰, it is now a common belief that this
456 channel adopts exclusively an asymmetric arrangement in absence of Mg²⁺.

457 NMR spectra are sensitive to the environments of each nucleus, and thus report on
458 conformational transitions breaking the local symmetries. The fact that the NMR fingerprint

459 spectra do not change significantly upon removal of Mg^{2+} indicates the conservation of local
460 symmetric environments for most of the NMR-active nuclei in both conditions. This evidence
461 in turn suggests that the global symmetry is maintained for a substantial population of CorA
462 pentamers, as it is unlikely that the ample rearrangements implied by the cryo-EM model could
463 occur without affecting local symmetries of so many nuclei in the five subunits. This view is
464 additionally corroborated by our negative-stain TEM data, which showed the presence of
465 nearly symmetric 2D classes in Mg^{2+} -free preparations.

466 Symmetry breaking is expected to result in local conformational heterogeneities between the
467 monomers, resulting in peak splitting, with a possible reduction of the intensity beyond the
468 detection limit. In this regard, the general decrease in intensity of the NMR spectra observed
469 in absence of Mg^{2+} suggests a significant reduction of the population of the observed
470 symmetric state, compatible with the co-existence of a broad distribution of asymmetric states.
471 It has previously been shown that CorA mutants with abolished M1 regulatory sites still
472 crystallize in a symmetric, closed state. This suggests that binding of Mg^{2+} is not necessary
473 for closing the channel¹⁹.

474 The two asymmetric cryo-EM structures were refined from only about 15 % each of the picked
475 particles, indicating the presence of various conformations, and possibly the symmetric form.
476 AFM provided a more detailed conformational analysis and found around 20% symmetric
477 structures at low Mg^{2+} concentrations (0-3 mM). The closely related Zn transporter ZntB also
478 showed a symmetric structure in the absence of regulatory cations⁴². All these observations
479 point towards a conformational equilibrium between the symmetric and various asymmetric
480 states which is partially but not entirely shifted towards asymmetric forms at low cation
481 concentration.

482

483 **Increased dynamics in CorA in absence of Mg^{2+} .** A “dynamic character” of CorA at low
484 levels of Mg^{2+} was postulated on the bases of the cryo-EM data²⁰ and recently characterized
485 by high-speed AFM²³. An elevated conformational plasticity would indeed be consistent with
486 the hitherto unsuccessful crystallization of a conducting state.

487 MAS NMR has the exclusive advantage of probing molecular motions with site-specific
488 resolution. Differently from a previous NMR study on a truncated construct in detergent
489 micelles⁴³, we here directly tackled the full-length protein in lipid bilayers. Notably, we
490 characterized the change in dynamics occurring upon Mg^{2+} release by acquiring NMR
491 observables sensitive to different timescales. On a fast ps-ns timescale, increased bulk ¹⁵N
492 R_1 s in the absence of Mg^{2+} are indicative of less restricted backbone motions, as also
493 suggested by MD simulations⁴¹. Site-specific ¹⁵N $R_{1\rho}$ rates are reporters of slower segmental
494 motions displacing secondary structure elements with respect to each other, over a window of

495 hundreds of ns to hundreds of μ s. These dynamical processes appear to be largely promoted
496 over the whole CorA structure when Mg^{2+} is absent.

497 Notably, a change in dynamics is also visible in the TMD region. Here we detected and
498 assigned most trans-membrane and periplasmic residues including the GMN motif in the
499 presence of Mg^{2+} . However, for these residues, peaks broadened beyond detection when Mg^{2+}
500 was removed. This points towards the presence of multiple conformations in this region as
501 well, although the exchange dynamics likely occurs on a different regime with respect to the
502 ICD domain. An earlier work suggested that removal of Mg^{2+} results in a combination of lateral
503 and radial tilting of two adjacent monomers, which allows the creation of interactions between
504 them¹². This idea was recently extended based on coarse-grained MD simulations that show
505 multi-step conformational changes propagating from the ICD to the TMD helices²². In line with
506 these observations, we propose that collective ns- μ s motions of the backbone initially
507 promoted in the ICD by release of Mg^{2+} ions would in turn induce higher conformational
508 flexibility in the TMD.

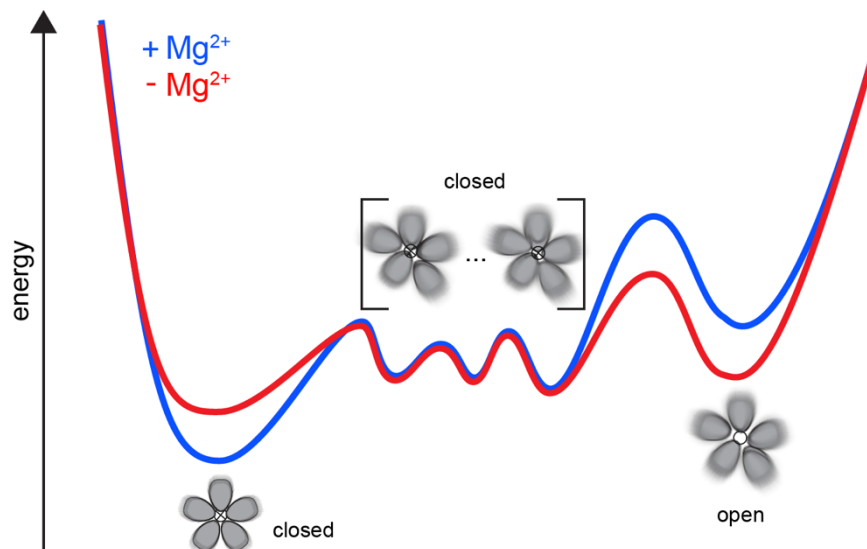
509

510 **Are all asymmetric states open/conductive? What is an open/conductive state?** Since
511 asymmetric structures are present both in presence and absence of Mg^{2+} , lack of symmetry is
512 not equivalent to conduction. The regulation of Mg^{2+} transport clearly needs to be dependent
513 on more stringent control. Interestingly, a previous MD study²¹ found that dry and intermediate
514 transiently wetted states, both non-conducting, were present both with and without bound Mg^{2+}
515 and interconversion rates on the ns time scale. Furthermore, in absence of Mg^{2+} , a conducting
516 “stably superhydrated” state was sampled, i.e. where the region of pore lining residues M291,
517 L294, A298, and M302 that form the main hydrophobic constriction is wetted by more than 20
518 water molecules. Though this state was only sampled in a minor part of the simulations, its
519 population could change at a longer time scale. Indeed, the ns sampled by the simulations
520 cannot describe our observations that CorA adopts symmetric and asymmetric conformations,
521 both in presence and absence of Mg^{2+} , while in absence of Mg^{2+} , the channel has higher
522 motional freedom on the μ s timescale. In light of the MD results, our combined findings support
523 the idea that the “stably superhydrated” state is present in low abundance and interconverts
524 rapidly with the remaining ensemble of states.

525

526 **An integrated view on CorA transport regulation.** Our findings cannot be explained in terms
527 of sharp transitions between open and closed states. An alternative model that integrates our
528 findings with the previously available literature is schematically illustrated in Figure 6. CorA
529 samples symmetric and asymmetric conformational states, whose distribution is tuned by the
530 Mg^{2+} concentration. Between the symmetric and open states, a relatively flat energy landscape
531 exists with asymmetric, closed states, both in the presence and absence of Mg^{2+} . Low Mg^{2+}

532 intracellular levels induce a reduction in the population of the symmetric, closed state together
533 with a decrease of the energy barrier towards the open state, which becomes more populated.
534 At these Mg^{2+} concentrations, CorA can visit a conducting asymmetric ensemble of states. In
535 this context, increased dynamics, as observed by NMR, can become the key determinant
536 allowing CorA to explore different wells of the energy profile, making the open state reachable.
537



538
539 **Figure 6** Schematic representations of a dynamic model for CorA. A complex landscape
540 connects a symmetric and closed state with an asymmetric open state, both in the presence
541 and in the absence of regulatory ions.

542 Such a dynamic model is equally compatible with previously unexplainable symmetric crystal
543 structures of M1-binding site mutants in the absence of Mg^{2+} ¹⁹. While for WT CorA, removal
544 of Mg^{2+} increases the dynamics and shifts the conformational equilibria, point mutations
545 probably have an opposite effect, stabilizing the symmetric state and allowing crystal
546 formation.

547
548 **Relating to other classes of proteins and channels.** Gating has been investigated
549 extensively in the family of pentameric ligand-gated ion channels (pLGIC)⁴⁴, which in general
550 have symmetric or pseudo-symmetric structures in the ligand-free form. Intriguingly, the
551 existence of asymmetric conformations has been observed in the absence of ligand for the
552 serotonin receptor 5HT3R, revealing conformational plasticity also in the resting state. Such
553 conformations are more energetically favorable when the agonist is bound, suggesting an
554 asymmetric activation where resting asymmetric states are possible intermediates of the
555 gating⁴⁵. Asymmetric activation was proposed also for the nicotinic receptor nAChR, where
556 the movement of pore lining helices was shown to induce the asymmetry in the ligand-bound
557 form⁴⁶. Taken together, these studies suggest that asymmetry might have a more widespread
558 occurrence in channel regulation. Asymmetric resting states may exist as intermediates in the

559 conformational landscape independently of the presence of substrate, but they become more
560 energetically favorable when this is bound.

561 Conclusion

562 The availability of room temperature SANS and NMR data of CorA in lipid bilayers, reporting
563 on both global and local behaviour of this channel, supported by MD simulations, allowed us
564 to extend and rationalise the “symmetry-break-upon-gating” model for Mg²⁺ transport. Our
565 observations support the suggestion that asymmetric conformations are involved in the gating
566 mechanism, but in a more complex way than a simpler two-state picture, where Mg²⁺ bound
567 CorA is a stable, symmetric structure. Indeed, we find that the CorA pentamer is a symmetry-
568 broken fluctuating structure able to explore a wide conformational landscape both in the
569 presence and absence of Mg²⁺. We propose that the determining factor for CorA to visit
570 conducting states is the increase in backbone flexibility on different timescales upon release
571 of regulatory Mg²⁺. Future investigations of the conformational equilibria will enrich the insight
572 provided in this study with a better mechanistic understanding of the kinetics and
573 thermodynamics of gating and transport.

574 Materials and methods

575 **Materials**

576 All chemicals were from Sigma-Aldrich unless otherwise stated. DDM was from Carbosynth
577 (UK), match-out-deuterated DDM (sDDM²⁹) and match-out deuterated POPC (d-POPC) were
578 synthesised at the National Deuteration Facility at ANSTO (Lucas Heights, Australia). The d-
579 POPC was synthesised as previously⁴⁷, but with custom deuteration (94% D in tail groups, 71
580 %D in head group). Details of the synthesis and chemical and isotopic analysis is described
581 below.

582

583 **Protein production and purification**

584 For SANS, CorA was produced and purified essentially as described elsewhere⁴⁸. For studies
585 in DDM, the N-terminal His-tag was cleaved by tobacco etch virus (TEV) protease before gel
586 filtration, whereas for nanodiscs, it was cleaved after incorporation (see below). For NMR,
587 uniformly isotopically labelled CorA was produced in M9 medium containing 3 g/L ¹³C-glucose
588 and 1 g/L ¹⁵N-ammonium chloride. ¹⁵N-alanine labelled CorA was produced in M9 medium
589 containing regular ¹²C-glucose and ¹⁴N-ammonium chloride and supplemented with 200 mg/L
590 of ¹⁵N-alanine. Match-out deuterated circularised membrane scaffold protein (MSP), d-

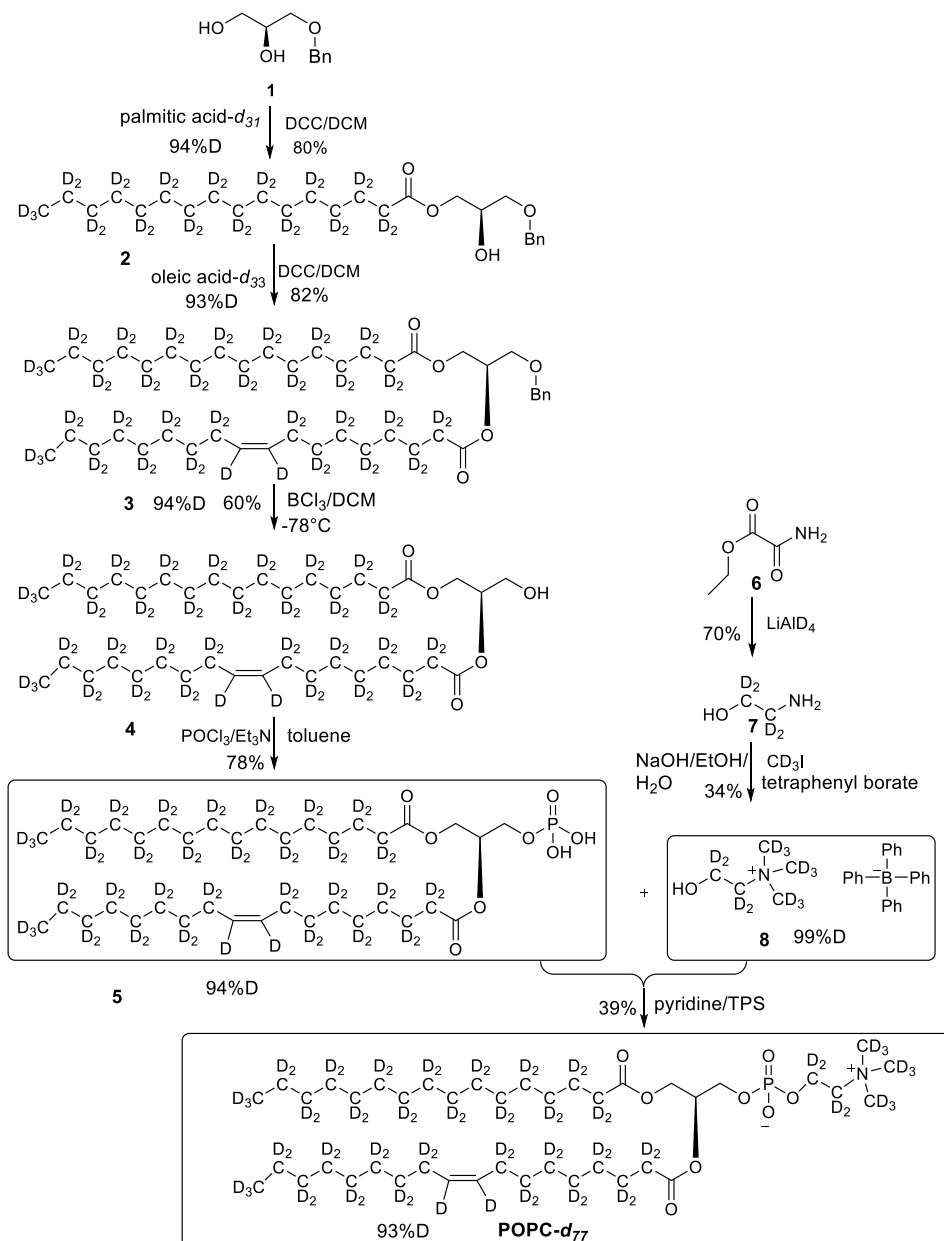
591 csMSP1E3D1, was produced at the D-lab at ILL (Grenoble, France) and purified as described
592 previously⁴⁸. Proteins were stored at -80 °C until used.

593

594 **Synthesis of match-out deuterated POPC**

595 The overall synthesis of POPC-*d*₇₇ is reported elsewhere⁴⁷. Figure 7 shows the synthetic
596 scheme followed in this study to produce the specific level of deuteration in the head and tail
597 groups of the POPC. The specific level of deuteration in the tail group was achieved by diluting
598 pure heavy water with light water in specific ratios in the Parr reactor when making the
599 deuterated alkyl chains from their fatty acid precursors²⁹. The analysis data and spectra of the
600 intermediate compounds and the final compound are shown in Figure 7-figure supplements 1
601 to 23. Electrospray ionisation mass spectra (ESI-MS) were recorded on a 4000 QTrap AB
602 SCIEX Mass Spectrometer. The overall percent deuteration of the molecules was calculated
603 by ER-MS (enhanced resolution – MS) using the isotope distribution analysis of the different
604 isotopologues by analysing the area under each MS peak which corresponds to a defined
605 number of deuterium atoms. The contribution of the carbon-13 (natural abundance) to the
606 value of the area under each [X+1] MS signal is subtracted based on the relative amount found
607 in the protonated version. In a typical analysis we measure the C-13 natural abundance
608 contribution by running ER-MS of the protonated version (or estimate it by ChemDraw
609 software) and use this value in our calculation using an in-house developed method that
610 subtracts this contribution from each MS signal constituting the isotope distribution. ¹H NMR
611 (400 MHz), ¹³C NMR (100 MHz), ³¹P NMR (162 MHz) and ²H NMR (61.4 MHz) spectra were
612 recorded on a Bruker 400 MHz spectrometer at 298 K. Chemical shifts, in ppm, were
613 referenced to the residual signal of the corresponding solvent. Deuterium NMR spectroscopy
614 was performed using the probe's lock channel for direct observation.

615



616

617 **Figure 7** Overall synthesis achieved by following a reported paper, all the intermediates and
 618 final POPC- d_{77} were obtained in similar yields⁴⁷.

619 **Figure supplement 1** ^1H NMR of 1-palmitoyl- d_{31} -sn-3-benzyloxy-glycerol (Figure 7, molecule
 620 2) in CDCl_3 . (400 MHz, CDCl_3), δ residual protons 0.88 (m, 0.22H), 1.10-1.7 (m, 1.96H),
 621 1.57-1.86 (m, 1.55H), 1.96 (m, 0.54H), 3.69 (m, 2H), 4.09 (m, 1H), 4.22 (m, 2H) 4.60 (s, 2H),
 622 7.36 (m, 5H).

623 **Figure supplement 2** ^2H NMR of 1-palmitoyl- d_{31} -sn-3-benzyloxy-glycerol (Figure 7, molecule
 624 2) in CDCl_3 . (400 MHz, CDCl_3), δ 0.82 (m), 1.18 (m), 1.54 (m), 2.27 (m).

625 **Figure supplement 3** ^{13}C NMR of 1-palmitoyl- d_{31} -sn-3-benzyloxy-glycerol (Figure 7, molecule
 626 2) in CDCl_3 . (400 MHz, CDCl_3), 10.9 (m), 22.09 (m), 28.33 (m), 33.05 (m), 65.33, 68.9, 70.80,
 627 73.5, 127.7, 127.9, 128.5, 137.6, 174.0.

628 **Figure supplement 4** ^1H NMR of 1-palmitoyl- d_{31} -2-oleoyl- d_{33} -sn-3-benzyloxy-glycerol (Figure
 629 7, molecule 3) in CDCl_3 . (400 MHz, CDCl_3), δ residual protons 0.90 (m, 3.56H), 1.29 (m,
 630 5.15H), 1.98 (m, 0.68H), 2.29 (m, 1.25H), 3.61 (d, $J = 5.0\text{Hz}$, 2H), 4.21 (m, 1H), 4.36 (m, 1H),

631 protonated benzyl protons 4.56 (AB q, $J = 12\text{Hz}$, 2H), 5.26 (m, 1H), 5.35 (s, 0.65H), 7.34 (m,
632 5H).

633 **Figure supplement 5** ^2H NMR of 1-palmitoyl- d_{31} -2-oleoyl- d_{33} -sn-3-benzyloxy-glycerol (Figure
634 7, molecule 3) in CDCl_3 . (400 MHz, CDCl_3), δ 0.82 (m, 6D), 1.19 (m, 35.35D), 1.53 (m, 3.74D),
635 1.94 (m, 3.34D), 2.25 (m, 2.63D), 3.56 (m, 1.71D), 4.27 (m, 1.04D), 5.35 (m, 1.92)

636 **Figure supplement 6** ^{13}C NMR of 1-palmitoyl- d_{31} -2-oleoyl- d_{33} -sn-3-benzyloxy-glycerol
637 (Figure 7, molecule 3) in CDCl_3 . (400 MHz, CDCl_3), δ 13.08 (m), 21.60 (m), 23.96 (m), 26.50
638 (m), 28.2 (m), 30.60 (m), 33.80 (m), 62.60, 68.39 9, 70.10, 73.1, 127.7, 127.9, 128.5, 137.7,
639 173.1, 173.4.

640 **Figure supplement 7** ESI-MS, m/z 749 $[\text{M}^{+1}]^+$ of POPC precursor 1-palmitoyl-2-oleoyl-sn-
641 benzyloxyglycerol- d_{64} (Figure 7, molecule 3). Overall 94%D, isotope distribution d_{64} , 7.8%, d_{63} ,
642 15.1%, d_{62} , 19.5%, d_{61} , 18.0%, d_{60} , 13.1%, d_{59} , 10.2%, d_{58} , 6.5%, d_{57} , 3.9%, d_{56} , 2.7%.

643 **Figure supplement 8** ^1H NMR of 1-palmitoyl- d_{31} -2-oleoyl- d_{33} -sn-3-glycerol (Figure 7,
644 molecule 4) in CDCl_3 . (400 MHz, CDCl_3), δ residual protons 0.24 (m, 0.47H), 1.28 (m, 1.51H),
645 1.67 (m, 2.24H), 2.13 (m, 0.52H), 2.23 (m, 1.29H), 3.72 (m, 2H), 4.30 (m, 2H), 5.10 (m, 1H),
646 5.34 (s, 0.48H).

647 **Figure supplement 9** ^2H NMR of 1-palmitoyl- d_{31} -2-oleoyl- d_{33} -sn-3-glycerol (Figure 7,
648 molecule 4) in CDCl_3 . (400 MHz, CDCl_3), δ 0.82 (m, 8.6D), 1.19 (m, 49.2D), 1.55 (m, 4.8D),
649 1.94 (m, 3.46D), 2.28 (m, 3.82D), 5.38 (m, 1.1D).

650 **Figure supplement 10** ^{13}C NMR of 1-palmitoyl- d_{31} -2-oleoyl- d_{33} -sn-3-glycerol (Figure 7,
651 molecule 4) in CDCl_3 . (400 MHz, CDCl_3), δ 12.89 (m), 21.39 (m), 22.6 (m), 24.00 (m), 26.25
652 (m), 28.2 (m), 30.49 (m), 33.86 (m), 65.00, 60.76, 61.60, 71.64, 128.02, 129.14, 129.5, 173.53,
653 173.93.

654 **Figure supplement 11** ^1H NMR of crude product 1-palmitoyl- d_{31} -2-oleoyl- d_{33} -sn-3-glycero-
655 phosphatidic acid (Figure 7, molecule 5) in CDCl_3 . This synthesised crude dried product was
656 used in next step without further purification.

657 **Figure supplement 12** ^{31}P NMR of crude product 1-palmitoyl- d_{31} -2-oleoyl- d_{33} -sn-3-glycero-
658 phosphatidic acid (Figure 7, molecule 5) in CDCl_3 . This synthesised crude dried product was
659 used in next step without further purification.

660 **Figure supplement 13** ESI-MS, m/z 737 $[\text{M}^{-1}]^-$ of crude product of 1-palmitoyl- d_{31} -2-oleoyl-
661 d_{33} -sn-3-glycero-phosphatidic acid (Figure 7, molecule 5). Overall 94%D, isotope distribution
662 d_{64} , 0.6%, d_{63} , 8.9%, d_{62} , 18.8%, d_{61} , 25.1%, d_{60} , 20.6%, d_{59} , 13.0%, d_{58} , 7.5%, d_{57} , 5.2%, d_{56} ,
663 0.2%, d_{55} , 0.1%.

664 **Figure supplement 14** ^1H NMR of POPC- d_{77} in CDCl_3 . (400 MHz, CDCl_3), δ residual protons
665 0.85 (m, 0.17H), 1.25 (m, 1.48H), 1.54 (m, 0.22H), 1.97 (m, 0.18H), 2.22 (m, 0.66H), 3.89 (m,
666 2H), 4.08 (m, 1H), 4.34 (m, 1H), 5.14 (m, 1H), 5.27 (s, 0.43H)

667 **Figure supplement 15** ^2H NMR of POPC- d_{77} in CDCl_3 . (400 MHz, CDCl_3), δ 0.80 (m), 1.19
668 (m), 2.20 (m), 1.93 (m, 6.0D), 3.35 (m), 3.84 (m), 5.36 (m).

669 **Figure supplement 16** ^{13}C NMR of POPC- d_{77} in CDCl_3 . (400 MHz, CDCl_3), δ 13.03 (m), 21.48
670 (m), 23.88 (m), 26.24 (m), 28.36 (m), 30.49 (m), 33.72 (m), 53.17, 58.76 (m), 62.24 (m), 69.84
671 (m), 127.90 (s), 129.5, 173.31, 173.69

672 **Figure supplement 17** $\{^1\text{H}\}$ and $\{^2\text{H}\}$ decoupled ^{13}C NMR spectra of POPC- d_{77} in CDCl_3 .

673 **Figure supplement 18** ^{31}P NMR of POPC- d_{77} in CDCl_3 . (400 MHz, CDCl_3), single peak at δ
674 -2.20

675 **Figure supplement 19** ESI-MS, m/z 838 $[M^{+1}]^+$ of POPC- d_{77} . Overall 93%D, isotope
676 distribution d_{77} , 0%, d_{76} , 0%, d_{75} , 7.5%, d_{74} , 21.2%, d_{73} , 28.7%, d_{72} , 25.3%, d_{71} , 15.5%, d_{70} ,
677 10.8%.

678 **Figure supplement 20** 1H NMR of choline- d_{13} tetraphylborate (Figure 7, molecule 8) in
679 DMSO- d_6 . (400 MHz, DMSO- d_6) δ 6.85 (m, 4H), 6.96 (m, 8H), 7.21 (m, 8H).

680 **Figure supplement 21** 2H NMR of choline- d_{13} tetraphylborate (Figure 7, molecule 8) in
681 DMSO- d_6 . (61.4 MHz, DMSO- d_6) δ 3.30 (m, 9D), 3.32 (m, 2D), 3.78 (m, 2D).

682 **Figure supplement 22** ^{13}C NMR of choline- d_{13} tetraphylborate (Figure 7, molecule 8) in
683 DMSO- d_6 . (100 MHz, DMSO- d_6) δ 52.5 (m), 54.9 (m), 121.9, 125.9, 136.2, 163.9 (m).

684 **Figure supplement 23** POPC- d_{77} percentage distribution of D levels at different sites.

685

686 **CorA reconstitution in sND for SANS**

687 CorA, d-csMSP1E3D1, and d-POPC solubilized in cholate were mixed in a ratio of 400:4:1
688 with a final d-POPC concentration of 10 mM. Cholate and DDM were removed by adding 50
689 % w/v amberlite XAD-2 overnight at 5 °C. CorA-loaded sNDs were purified by IMAC on NiNTA
690 resin, added TEV protease and dialysed for three hours at RT followed by ON dialysis at 4 °C
691 against 20 mM TrisHCl pH 8, 100 mM NaCl, 0.5 mM EDTA, 1 mM DTT. Finally, the cleaved
692 sample was purified by reverse IMAC on NiNTA resin. The sample was concentrated to
693 approximately 30 μ M before the SANS experiment.

694

695 **Reconstitution into multilamellar vesicles for NMR**

696 CorA was reconstituted into DMPC at a lipid-to-protein ratio of 0.5 (w/w) by dialysis against 10
697 mM Tris-HCl pH 8, 40 mM $MgCl_2$, 1 mM methyl- β -cyclodextrin using a 25 kDa MWCO
698 membrane at RT. A white precipitate of multilamellar vesicles was visible after 48 hours and
699 collected by centrifugation after 72 hours. Samples were packed into 1.3 mm or 0.7 mm MAS
700 NMR rotors using an ultracentrifuge tool (Giotto Biotech) at 100.000g for 1 hour.

701

702 **SEC-SANS**

703 Samples were measured at the D22 beamline at ILL, using the SEC-SANS mode described
704 elsewhere^{26,27}, but with the upgrade that UV absorption was measured on the flow cell in the
705 same place, but perpendicular to the neutron beam. The setup was placed in a temperature-
706 controlled cabinet at 11 °C. CorA in sDDM was run on a Superdex200 Increase 10/300 GL
707 column (GE Healthcare) in 20 mM TrisDCI pH 7.5, 150 mM NaCl, 1 mM DTT, 0.5 mM sDDM
708 in D_2O with an initial flow rate of 0.3 ml/min to allow full exchange into s-DDM²⁹. CorA in sND
709 was run on a Superose6 Increase 10/300 GL column (GE Healthcare) in 20 mM TrisDCI pH
710 7.5, 150 mM NaCl, 1 mM DTT in D_2O with an initial flow rate of 0.5 ml/min. For all samples,
711 the flow was reduced to 0.05 ml/min during elution of the main peak. Measurements were run
712 twice to obtain data from two sample-to-detector distances, 2 m and 11 m, yielding data in a

713 q -range of 0.0044 \AA^{-1} to 0.42 \AA^{-1} with the neutron wavelength of 6 \AA . The scattering intensity,
714 $I(q)$, was brought to absolute scale in units of cm^{-1} by normalizing to the direct beam intensity
715 measured with an attenuator in place.

716

717 Pair distance, $p(r)$, distributions were calculated by Bayesian indirect Fourier transformation
718 at the bayesapp server³² (available from the genapp server at
719 <https://somo.chem.utk.edu/bayesapp/>). $p(r)$ s and the corresponding $I(q)$ s for PDB structures
720 were calculated using CaPP (available at [github.com/Niels-Bohr-Institute-XNS-](https://github.com/Niels-Bohr-Institute-XNS-StructBiophys/CaPP)
721 [StructBiophys/CaPP](https://github.com/Niels-Bohr-Institute-XNS-StructBiophys/CaPP)) with a water layer excess density of 6 % applied to the parts of the
722 protein outside the membrane.

723

724 **Model building**

725 For use in both SANS comparison, normal mode analysis, and simulations, we rebuilt the
726 missing residues and sidechains of the closed PDB structure 4I0U. The 2-6 missing residues
727 at each chain terminal was rebuilt using Modeller's automodel functionality⁴⁹. In the open cryo-
728 EM structures, between 18-20 residues were missing in the N-terminal. These were rebuilt
729 from the closed X-ray structure (4I0U) to allow for direct comparison to SANS measurements.

730

731 **Normal mode analysis**

732 Non-linear normal mode analysis was performed using the NOn-Linear rigid Block NMA⁵⁰
733 (NOLB) routine (available from <https://hal.inria.fr/hal-01505843v2>). The NOLB routine was
734 integrated with PEPSI-SANS 2.2 (<https://team.inria.fr/nano-d/software/pepsi-sans/>) and a
735 regularization algorithm to avoid unphysical structures. In the latter, $T = \chi^2 + \alpha S$ is minimized,
736 where S constraints the secondary structure deviation. Scanning over different values of α , a
737 plot of χ^2 vs. S is obtained. The best compromise between conservation of structure and the
738 best fit to the data is chosen from the "elbow"-region (Figure 4-figure supplement 2).

739

740 **Metadynamics and reweighting**

741 The simulation system was set up using the MARTINI3.0b coarse grained force field⁵¹ with
742 elastic networks terms applied to the individual chains only with a 0.9 nm cut-off and a force
743 constant of $500 \text{ kJ}/(\text{mol nm}^2)$. As MARTINI does not contain parameters for protein bound
744 Mg^{2+} but rather models it as a free ligand with four waters bound, the Mg^{2+} ions bound in the
745 structure were deleted. To avoid overly electrostatic repulsions from the remaining Mg^{2+}
746 coordinating amino acids (Asp89, Asp179, Asp253 and Glu88), they were transformed into
747 their protonated states. The POPC membrane was obtained from CHARMM-GUI^{52,53} using
748 450 POPCs in each bilayer, ensuring and the entire system was big enough for larger

749 conformational changes. The system was solvated with the MARTINI non-polarizable water
750 and neutralized with 300 mM NaCl comparable to the SANS experimental set-up. The
751 equilibration was performed according to the CHARMM-GUI equilibration protocol using a
752 minimization step followed by 6 equilibration steps with slow decrease in the positional
753 restraint forces on both lipids and protein in each step⁵³.

754

755 The GROMACS-5.1.4 software package⁵⁴ was used to simulate with a 20 fs time step.
756 Temperature and semi-isotropic pressure were controlled at 303.15 K and 1 bar using the
757 stochastic velocity rescaling thermostat⁵⁵ and Parrinello-Rahman barostat⁵⁶. Electrostatic
758 interactions were modulated using the reaction field approach. The cutoff of short-range
759 distance for the electrostatic interactions was 1.1 nm. The potential shift Verlet scheme was
760 used to cut off the Lennard-Jones potential at long ranges.

761

762 Well-Tempered Metadynamics⁵⁷ simulations were performed with the PLUMED2.3.0
763 software⁵⁸. A radius of gyration collective variable was applied on all back- bone beads for the
764 intracellular residues 170 190 and 220 250 of all 5 chains. The metadynamics parameters
765 were set as follows: Gaussian width = 0.05, Gaussian height = 2.1, Gaussian de- position
766 stride = 100, biasfactor = 15 and an upper wall defined at a CV radius of gyration of 4.0 nm.
767 The wall was defined as a harmonic restraint with a force constant = 10000, harmonic
768 exponential power = 4, off-set = 0, and a rescaling factor of 1. Multiple wall types and sizes
769 was attempted with lower walls causing too little dynamics for fitting with the experimental
770 SANS data and higher walls causing individual monomers to bend unphysically and giving
771 unfeasible large sample space. Clustering of the simulation trajectory was performed using
772 the KMeans clustering method⁵⁹.

773

774 The software program BME was used reweight the MetaD trajectory to fit the experimental
775 SANS data⁶⁰. The hyperparameter θ was determined based on a L-curve analysis (analogous
776 to the procedure in normal mode analysis, see Figure 4-figure supplement 2) of S_{rel} vs χ^2 ,
777 where θ is chosen where a natural kink is observed and any further decrease in χ^2 gives rise
778 to an increasing larger penalty in S_{rel} . As the simulations are not fully converged and the
779 chosen force field is coarse grained, we set the trust in the force field lower and chose a slightly
780 lower θ -value than the kink observed.

781

782 To account for a fixed fraction of symmetric pentamers, a differential intensity was derived by
783 $I_{diff} = I_{exp} - f \cdot I_{calc, 5sym}$, where f is the fraction of symmetric pentamer, I_{exp} is the experimental
784 SANS data, and $I_{calc, 5sym}$ is the SANS signal of PDB 4I0U calculated by PEPSI-SANS. The

785 forward scattering of the calculated SANS signal, $I_{\text{calc},5\text{sym}}(0)$, was scaled to match the forward
786 scattering of the experimental SANS data. Reweighting was done against the differential
787 SANS signal.

788

789 **Solid-state NMR Spectroscopy**

790 Spectra of uniformly labelled samples were measured at a magnetic field of either 19.5 T or
791 23.4 T corresponding to a ^1H Larmor frequency of 800 MHz and 1000 MHz, respectively. The
792 spectrometers were equipped with a Bruker 0.7 mm MAS probe, spinning at 107 kHz, at a
793 constant temperature of 300 K. Spectra of ^{15}N Ala labelled samples were acquired at 23.4 T
794 on a Bruker 1.3 mm MAS probe, spinning at 60 kHz, at a constant temperature of 300 K. The
795 assignment of backbone resonances was preliminary obtained by acquiring a set of ^1H -
796 detected 3D experiments as described in ^{61,62}. Adamantane was used as the external
797 reference. Spectral analysis and assignment were accomplished with CcpNmr Analysis ⁶³ and
798 FLYA ⁶⁴.

799 Relaxation experiments were based on a $^1\text{H},^{15}\text{N}$ ^1H -detected CP-HSQC experiment
800 incorporating an appropriate relaxation delay⁶⁵. 38 and 33 residues spanning different regions
801 of the proteins were used for the uniformly labelled sample in the presence and in the absence
802 of Mg^{2+} , respectively. The measurements of site-specific ^{15}N $R_{1\rho}$ rates were performed at 107
803 kHz MAS, 19.5 T and 300 K and 280 K, using relaxation delays of 0.05, 1, 5, 15, 50, 100, 200
804 ms under a spin-lock field of 15 kHz. Measurements of bulk ^{15}N R_1 were performed at 107
805 kHz MAS, 19.5 T and 300 K, using relaxation delays of 0.5, 1, 2.8, 6.8, 15.8, 23.8, 53.5, 80 s.
806 Measurements of ^{15}N $R_{1\rho}$ rates were additionally performed on the ^{15}N Ala labelled samples
807 in the presence and in the absence of Mg^{2+} at 60 kHz MAS, 23.5 T and 300 K using relaxation
808 delays of 0.1, 1, 5, 10, 25, 50, 100 ms under a spin-lock field of 15 kHz. The relaxation rates
809 were obtained by fitting the experimental decay curves with a mono-exponential function. The
810 error was estimated from the experimental noise by use of a Monte-Carlo evaluation.

811

812 **Activity assay**

813 Large unilamellar vesicles of POPC were prepared by dissolving a lipid film in 10 mM MOPS-
814 KOH pH 7.2, 150 mM KCl, 100 μM EGTA including 10 μM Mag-Fluo-4 (Thermo) to a POPC
815 concentration of 15 mg/ml, which was extruded through 0.2 μm membrane filters for 35 times
816 using a mini-extruder (Avanti Polar Lipids). CorA was inserted by mixing a sample of 10.5
817 mg/ml LUVs, 2 μM CorA, 10 μM Mag-Fluo-4 and 50 mM octyl glucoside. Biobeads SM-2 were
818 added to 45 % w/v and incubated at RT for 30 min, before purifying and at the same time
819 exchanging the extravesicular buffer to measurement buffer (10 mM MOPS-KOH pH 7.2, 150
820 N-methyl-D-glucamine-HCl, 100 μM EGTA) on Sephadex G50 resin. 20 μl of CorA-LUVs (or
821 plain LUVs) were diluted to a total of 1 ml in measurement buffer (prepared in H_2O or D_2O ,

822 respectively) containing 10 μM valinomycin with or without 1 mM $\text{Co}[\text{NH}_3]^{3+}$ present. CorA
823 activity was monitored by Mag-Fluo-4 fluorescence at 515 nm (excitation at 488 nm) on a
824 FluoroMax fluorometer (Horiba) upon addition of 10 mM MgCl_2 (from a 1 M stock prepared in
825 H_2O or D_2O , respectively). The signal was normalized to the flat signal recorded before
826 addition of MgCl_2 .

827

828 **Negative stain EM**

829 CorA was purified by SEC and diluted to 0.1 μM in appropriate buffers containing 1 mM EDTA
830 or 40 mM Mg^{2+} . Copper grids were neutralized with an Easiglow glow discharger (Agar
831 Scientific). 3 μl of sample was applied to the grid and incubated for 30 s. The grid was blotted
832 onto a filter paper from the edge, and 3 μL of 2% uranyl formate was added immediately and
833 incubated for 30 s. The staining procedure was repeated two more times. After the final
834 staining, the grid was left to dry for ten minutes. EM data were acquired on a Tecnai TEM (FEI,
835 Thermo Fischer scientific) at Aarhus University, Denmark. The micrographs were processed
836 by XMIPP to *.mcp files, and particle picking, 2D class averages and 3D model refinement
837 was done in Relion 3.0. Statistics for the 3D refinement are given in Table 1.

Parameter	1 mM EDTA	40 mM MgCl_2
Pixel size, \AA	3.14	3.14
Number of micrographs	436	440
Number of picked particles	193606	185577
Final number of particles	36176	46544
Resolution, \AA	≈ 15	≈ 15

838 Table 1 Negative stain EM statistics for 3D model refinement.

839 **Acknowledgements**

840 We thank Elliot Gilbert for his assistance with SANS experiments at QUOKKA at ANSTO and
841 Marta Brennich for her assistance with SAXS experiments at BM29 at the ESRF. Thomas
842 Boesen is acknowledged for his help with EM experiments conducted at Aarhus University
843 and Michael Gajhede for his assistance in EM data processing. We thank Ida Louise
844 Jørgensen for helping with functional reconstitution of CorA in large unilamellar vesicles and
845 Michael Maguire for providing a plasmid encoding CorA.

846 Additional information

847 Funding

Funder	Grant reference number	Author
Lundbeck Foundation: Brainstruc	R155-2015-2666	LA, KLL
Novo Nordisk Foundation: Synergy	NNF15OC0016670	LA
ERC: European Union's Horizon 2020 research and innovation programme	ERC-2015-CoG GA 648974	GP
BBSRC	BB/R00126X/1; BB/N000145/1	MS
EPSRC	EP/R004722/1; EP/R029407/1; EP/V010948/1	MS
Wellcome Trust	208361/Z/17/Z	MS
National Collaborative Research Infrastructure Strategy		TD
European Commision iNext Discovery	GA 871037	TS
Villum Fonden	35955	NTJ

848

849 Competing interests

850 The authors declare no competing interests.

851

852 Author Contributions

853 LA, GP and KLL conceived the project. NTJ, JB, NY, and TS prepared samples. NTJ, AHL,
854 FGT, PH, AM, and MCP carried out SANS experiments and modeling. NTJ and TGP carried
855 out activity measurements. NTJ and AHL did EM experiments. TB, AHL, and RC carried out
856 simulations. MB, AB, and TS carried out NMR experiments and modeling. LA, GP, KLL, MR,
857 TGP, TD, and MS supervised the research. NTJ, MB, TS, LA, GP and KLL wrote the
858 manuscript with input from all authors.

859

860 Data availability

861 The SANS data have been deposited to the Small Angle Scattering Biological Data Bank
862 (<https://www.sasbdb.org/>, access codes SASDM42, SASDM52, SASDM62, SASDM72). The
863 NMR resonance assignments have been deposited in the Biological Magnetic Resonance
864 Data Bank (<https://bmr.io>, access code 50959). The EM maps have been deposited to the
865 Electron Microscopy Data Bank (<https://www.ebi.ac.uk/emdb>, access codes EMD-13326 and
866 EMD-13327). Fluorescence data on CorA activity are available at GitHub
867 <https://github.com/Niels-Bohr-Institute-XNS-StructBiophys/CorAData/>. The metadynamics

868 simulations are available at GitHub [https://github.com/KULL-](https://github.com/KULL-Centre/papers/tree/main/2021/CorA-Johansen-et-al)
869 [Centre/papers/tree/main/2021/CorA-Johansen-et-al](https://github.com/KULL-Centre/papers/tree/main/2021/CorA-Johansen-et-al).

870

871 **Current affiliations**

872 NTJ: Section for Transport Biology, Department of Plant and Environmental Sciences,
873 University of Copenhagen, Frederiksberg, Denmark

874 AB: Institut des Sciences et Ingénierie Chimiques, École Polytechnique Fédérale de
875 Lausanne (EPFL), Lausanne, Switzerland;

876 RC: CSIC-Institute for Advanced Chemistry of Catalonia (IQAC), Barcelona, Catalonia,
877 Spain.

878

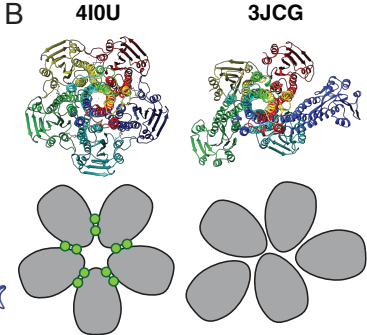
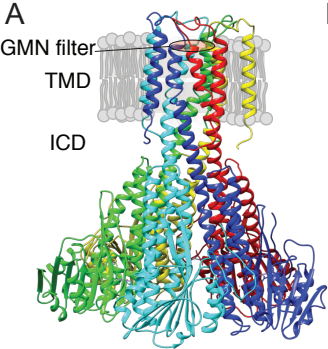
879 **References**

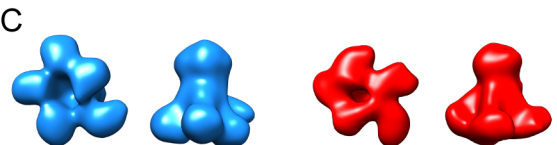
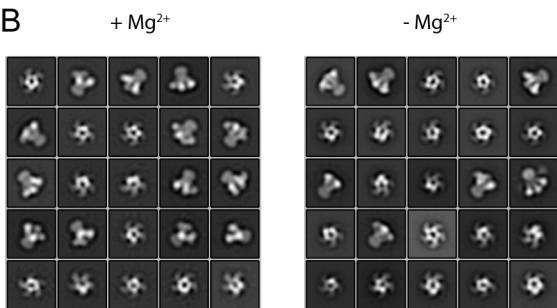
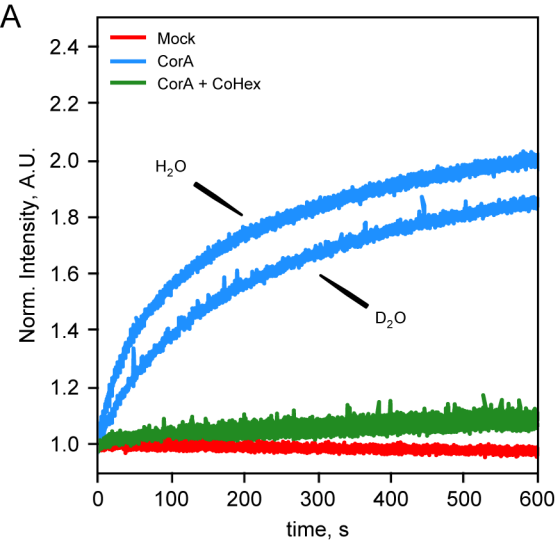
- 880 1. Jahnen-Dechent, W. & Ketteler, M. Magnesium basics. *Clinical Kidney Journal* **5**, i3–
881 i14 (2012).
- 882 2. Rude, R. K. Magnesium Deficiency: A Cause of Heterogenous Disease in Humans.
883 *Journal of Bone and Mineral Research* **13**, 749–758 (1998).
- 884 3. de Baaij, J. H. F., Hoenderop, J. G. J. & Bindels, R. J. M. Magnesium in man:
885 Implications for health and disease. *Physiological Reviews* **95**, 1–46 (2015).
- 886 4. Dinicolantonio, J. J., Liu, J. & O’Keefe, J. H. Magnesium for the prevention and
887 treatment of cardiovascular disease. *Open Heart* **5**, 1–10 (2018).
- 888 5. Maguire, M. E. Magnesium transporters: properties, regulation and structure. *Frontiers*
889 *in bioscience : a journal and virtual library* **11**, 3149–63 (2006).
- 890 6. Papp-Wallace, K. M. & Maguire, M. E. Bacterial homologs of eukaryotic membrane
891 proteins: The 2-TM-GxN family of Mg²⁺ transporters (Review). *Molecular Membrane*
892 *Biology* **24**, 351–356 (2007).
- 893 7. Knoop, V., Groth-Malonek, M., Gebert, M., Eifler, K. & Weyand, K. Transport of
894 magnesium and other divalent cations: Evolution of the 2-TM-GxN proteins in the MIT
895 superfamily. *Molecular Genetics and Genomics* **274**, 205–216 (2005).
- 896 8. Lunin, V. v *et al.* Crystal structure of the CorA Mg²⁺ transporter. *Nature* **440**, 833–837
897 (2006).
- 898 9. Eshaghi, S. Crystal Structure of a Divalent Metal Ion Transporter CorA at 2.9
899 Angstrom Resolution. *Science* **313**, 354–357 (2006).
- 900 10. Payandeh, J. & Pai, E. F. A structural basis for Mg²⁺ homeostasis and the CorA
901 translocation cycle. *EMBO Journal* **25**, 3762–3773 (2006).
- 902 11. Nordin, N. *et al.* Exploring the structure and function of *Thermotoga maritima* CorA
903 reveals the mechanism of gating and ion selectivity in Co²⁺ /Mg²⁺ transport.
904 *Biochemical Journal* **451**, 365–374 (2013).
- 905 12. Pföh, R. *et al.* Structural asymmetry in the magnesium channel CorA points to
906 sequential allosteric regulation. *Proceedings of the National Academy of Sciences*
907 **109**, 18809–18814 (2012).
- 908 13. Palombo, I., Daley, D. O. & Rapp, M. Why Is the GMN Motif Conserved in the
909 CorA/Mrs2/Alr1 Superfamily of Magnesium Transport Proteins? *Biochemistry* **52**,
910 4842–4847 (2013).

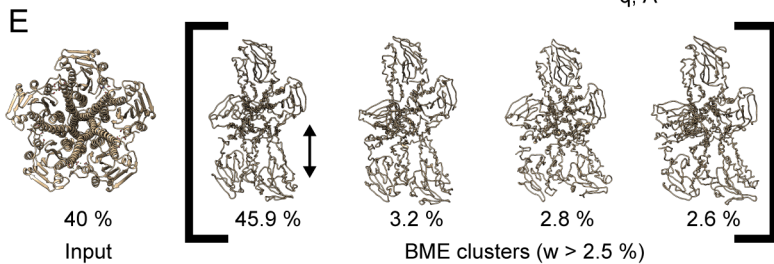
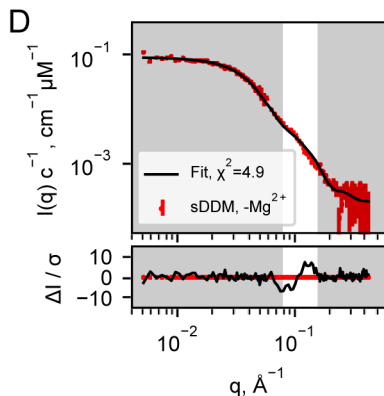
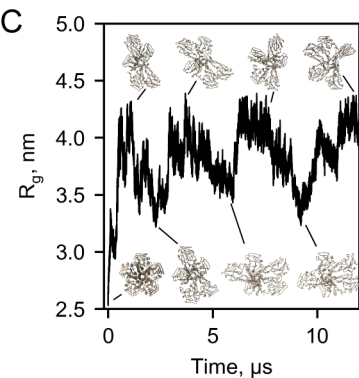
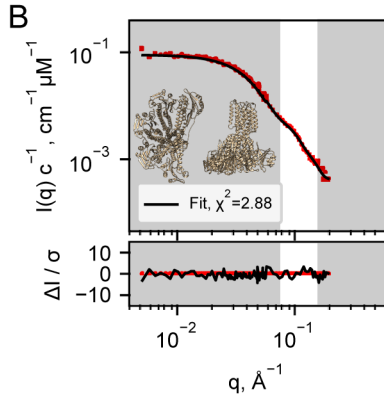
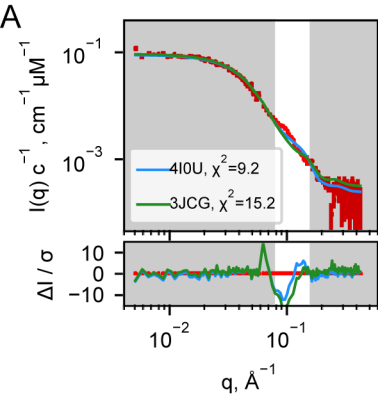
- 911 14. Dalmas, O. *et al.* A repulsion mechanism explains magnesium permeation and
912 selectivity in CorA. *Proceedings of the National Academy of Sciences* **111**, 3002–
913 3007 (2014).
- 914 15. Payandeh, J. *et al.* Probing Structure-Function Relationships and Gating Mechanisms
915 in the CorA Mg²⁺ Transport System. *Journal of Biological Chemistry* **283**, 11721–
916 11733 (2008).
- 917 16. Dalmas, O., Sompornpisut, P., Bezanilla, F. & Perozo, E. Molecular mechanism of
918 Mg²⁺-dependent gating in CorA. *Nature Communications* **5**, 3590 (2014).
- 919 17. Chakrabarti, N., Neale, C., Payandeh, J., Pai, E. F. & Pomès, R. An iris-like
920 mechanism of pore dilation in the CorA magnesium transport system. *Biophysical*
921 *Journal* **98**, 784–792 (2010).
- 922 18. Guskov, A. *et al.* Structural insights into the mechanisms of Mg²⁺ uptake, transport,
923 and gating by CorA. *Proceedings of the National Academy of Sciences* **109**, 18459–
924 18464 (2012).
- 925 19. Kowitz, T. & Maguire, M. E. BBA - General Subjects Loss of cytosolic Mg²⁺ binding
926 sites in the *Thermotoga maritima* CorA Mg²⁺ channel is not sufficient for channel
927 opening. *BBA - General Subjects* **1863**, 25–30 (2019).
- 928 20. Matthies, D. *et al.* Cryo-EM Structures of the Magnesium Channel CorA Reveal
929 Symmetry Break upon Gating. *Cell* **164**, 747–756 (2016).
- 930 21. Neale, C., Chakrabarti, N., Pomorski, P., Pai, E. F. & Pomès, R. Hydrophobic Gating
931 of Ion Permeation in Magnesium Channel CorA. *PLOS Computational Biology* **11**,
932 e1004303 (2015).
- 933 22. Nemchinova, M., Melcr, J., Wassenaar, T. A., Marrink, S. J. & Guskov, A. Asymmetric
934 CorA Gating Mechanism as Observed by Molecular Dynamics Simulations. *Journal of*
935 *Chemical Information and Modeling* [acs.jcim.1c00261](https://doi.org/10.1021/acs.jcim.1c00261) (2021)
936 doi:10.1021/acs.jcim.1c00261.
- 937 23. Rangl, M., Schmandt, N., Perozo, E. & Scheuring, S. Real time dynamics of gating-
938 related conformational changes in CorA. *eLife* **8**, 1–17 (2019).
- 939 24. Reif, B., Ashbrook, S. E., Emsley, L. & Hong, M. Solid-state NMR spectroscopy.
940 *Nature Reviews Methods Primers* **1**, 2 (2021).
- 941 25. Bonaccorsi, M., le Marchand, T. & Pintacuda, G. Protein structural dynamics by
942 Magic-Angle Spinning NMR. *Current Opinion in Structural Biology* **70**, 34–43 (2021).
- 943 26. Johansen, N. T., Pedersen, M. C., Porcar, L., Martel, A. & Arleth, L. Introducing SEC-
944 SANS for studies of complex self-organized biological systems. *Acta*
945 *Crystallographica Section D Structural Biology* **74**, 1178–1191 (2018).
- 946 27. Jordan, A. *et al.* SEC-SANS: size exclusion chromatography combined in situ with
947 small-angle neutron scattering. *Journal of Applied Crystallography* **49**, 2015–2020
948 (2016).
- 949 28. Maric, S. *et al.* Stealth carriers for low-resolution structure determination of membrane
950 proteins in solution. *Acta Crystallographica Section D Biological Crystallography* **70**,
951 317–328 (2014).
- 952 29. Midtgaard, S. R. *et al.* Invisible detergents for structure determination of membrane
953 proteins by small-angle neutron scattering. *FEBS Journal* **285**, 357–371 (2018).
- 954 30. Schubeis, T., le Marchand, T., Andreas, L. B. & Pintacuda, G. 1H magic-angle
955 spinning NMR evolves as a powerful new tool for membrane proteins. *Journal of*
956 *Magnetic Resonance* **287**, 140–152 (2018).

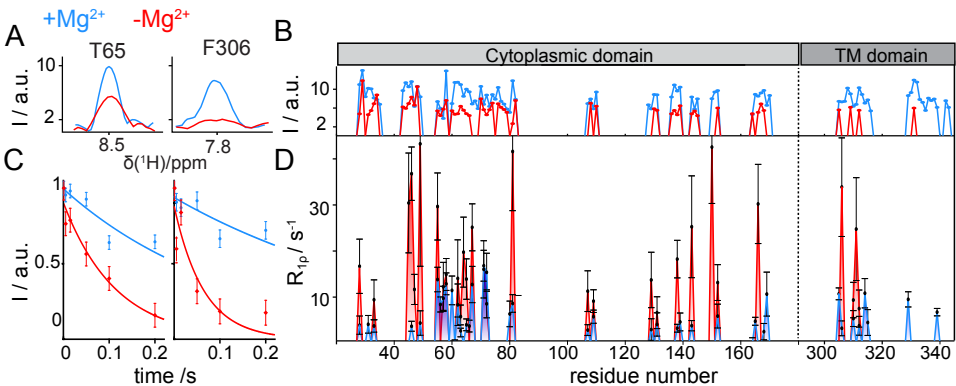
- 957 31. Schubeis, T. *et al.* A β -barrel for oil transport through lipid membranes: Dynamic NMR
958 structures of AlkL. *Proceedings of the National Academy of Sciences of the United*
959 *States of America* **117**, 21014–21021 (2020).
- 960 32. Hansen, S. Update for BayesApp : a web site for analysis of small-angle scattering
961 data. *Journal of Applied Crystallography* **47**, 1469–1471 (2014).
- 962 33. Skar-Gislinge, N. *et al.* Elliptical Structure of Phospholipid Bilayer Nanodiscs
963 Encapsulated by Scaffold Proteins: Casting the Roles of the Lipids and the Protein.
964 *Journal of the American Chemical Society* **132**, 13713–13722 (2010).
- 965 34. Pedersen, M. C., Arleth, L. & Mortensen, K. WilltFit : a framework for fitting of
966 constrained models to small-angle scattering data. *Journal of Applied Crystallography*
967 **46**, 1894–1898 (2013).
- 968 35. Némethy, G. & Scheraga, H. A. Structure of Water and Hydrophobic Bonding in
969 Proteins. IV. The Thermodynamic Properties of Liquid Deuterium Oxide. *The Journal*
970 *of Chemical Physics* **41**, 680–689 (1964).
- 971 36. Sugiyama, T. & Yoshiok, T. Functional Difference Between Deuterated and
972 Protonated Macromolecules. in *Protein Structure* (ed. Faraggi, E.) 291–308 (InTech,
973 2012). doi:10.5772/36649.
- 974 37. Hummer, G., Garde, S., García, A. E. & Pratt, L. R. New perspectives on hydrophobic
975 effects. *Chemical Physics* **258**, 349–370 (2000).
- 976 38. Franke, D. & Svergun, D. I. DAMMIF , a program for rapid ab-initio shape
977 determination in small-angle scattering. *Journal of Applied Crystallography* **42**, 342–
978 346 (2009).
- 979 39. Franke, D. *et al.* ATSAS 2.8: A comprehensive data analysis suite for small-angle
980 scattering from macromolecular solutions. *Journal of Applied Crystallography* **50**,
981 1212–1225 (2017).
- 982 40. Payandeh, J. & Pai, E. F. A structural basis for Mg²⁺ homeostasis and the CorA
983 translocation cycle. *The EMBO Journal* **25**, 3762–3773 (2006).
- 984 41. Chakrabarti, N., Neale, C., Payandeh, J., Pai, E. F. & Pomès, R. An iris-like
985 mechanism of pore dilation in the CorA magnesium transport system. *Biophysical*
986 *Journal* **98**, 784–792 (2010).
- 987 42. Gati, C., Stetsenko, A., Slotboom, D. J., Scheres, S. H. W. & Guskov, A. The
988 structural basis of proton driven zinc transport by ZntB. *Nature Communications* **8**,
989 1313 (2017).
- 990 43. Hu, J., Sharma, M., Qin, H., Gao, F. P. & Cross, T. A. Ligand Binding in the
991 Conserved Interhelical Loop of CorA, a Magnesium Transporter from Mycobacterium
992 tuberculosis. *Journal of Biological Chemistry* **284**, 15619–15628 (2009).
- 993 44. Rao, S., Klesse, G., Lynch, C. I., Tucker, S. J. & Sansom, M. S. P. Molecular
994 Simulations of Hydrophobic Gating of Pentameric Ligand Gated Ion Channels:
995 Insights into Water and Ions. *Journal of Physical Chemistry B* **125**, 981–994 (2021).
- 996 45. Zhang, Y. *et al.* Asymmetric opening of the homopentameric 5-HT_{3A} serotonin
997 receptor in lipid bilayers. *Nature Communications* **12**, 1074 (2021).
- 998 46. Unwin, N. & Fujiyoshi, Y. Gating Movement of Acetylcholine Receptor Caught by
999 Plunge-Freezing. *Journal of Molecular Biology* **422**, 617–634 (2012).
- 1000 47. Yepuri, N. R. *et al.* Synthesis of Perdeuterated 1-Palmitoyl-2-oleoyl- sn -glycero-3-
1001 phosphocholine ([D 82]POPC) and Characterisation of Its Lipid Bilayer Membrane
1002 Structure by Neutron Reflectometry. *ChemPlusChem* **81**, 315–321 (2016).

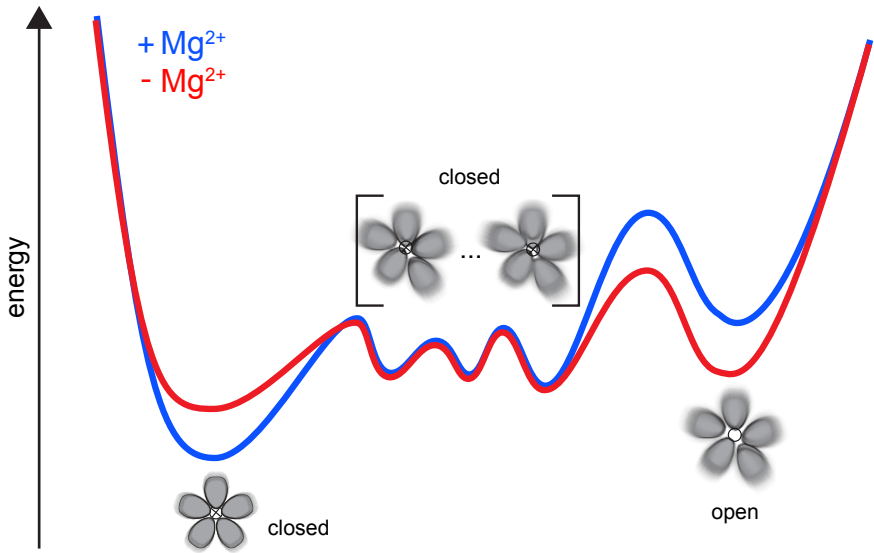
- 1003 48. Johansen, N. T. *et al.* Circularized and solubility-enhanced MSPs facilitate simple and
1004 high yield production of stable nanodiscs for studies of membrane proteins in solution.
1005 *The FEBS Journal* **0**, 1734–1751 (2019).
- 1006 49. Webb, B. & Sali, A. Protein Structure Modeling with MODELLER. in *Functional*
1007 *Genomics: Methods and Protocols* (eds. Kaufmann, M., Klinger, C. & Savelsbergh, A.)
1008 39–54 (Springer New York, 2017). doi:10.1007/978-1-4939-7231-9_4.
- 1009 50. Hoffmann, A. & Grudinin, S. NOLB: Nonlinear Rigid Block Normal-Mode Analysis
1010 Method. *Journal of Chemical Theory and Computation* **13**, 2123–2134 (2017).
- 1011 51. Marrink, S. J. Martini 3 open-beta release. <http://cgmartini.nl/index.php/martini3beta>.
- 1012 52. Jo, S., Lim, J. B., Klauda, J. B. & Im, W. CHARMM-GUI Membrane Builder for Mixed
1013 Bilayers and Its Application to Yeast Membranes. *Biophysical Journal* **97**, 50–58
1014 (2009).
- 1015 53. Qi, Y. *et al.* CHARMM-GUI Martini Maker for Coarse-Grained Simulations with the
1016 Martini Force Field. *Journal of Chemical Theory and Computation* **11**, 4486–4494
1017 (2015).
- 1018 54. Abraham, M. J. *et al.* GROMACS: High performance molecular simulations through
1019 multi-level parallelism from laptops to supercomputers. *SoftwareX* **1–2**, 19–25 (2015).
- 1020 55. Bussi, G., Donadio, D. & Parrinello, M. Canonical sampling through velocity rescaling.
1021 *The Journal of Chemical Physics* **126**, 014101 (2007).
- 1022 56. Parrinello, M. & Rahman, A. Polymorphic transitions in single crystals: A new
1023 molecular dynamics method. *Journal of Applied Physics* **52**, 7182–7190 (1981).
- 1024 57. Barducci, A., Bussi, G. & Parrinello, M. Well-Tempered Metadynamics: A Smoothly
1025 Converging and Tunable Free-Energy Method. *Physical Review Letters* **100**, 020603
1026 (2008).
- 1027 58. Tribello, G. A., Bonomi, M., Branduardi, D., Camilloni, C. & Bussi, G. PLUMED 2: New
1028 feathers for an old bird. *Computer Physics Communications* **185**, 604–613 (2014).
- 1029 59. Tiberti, M., Papaleo, E., Bengtson, T., Boomsma, W. & Lindorff-Larsen, K. ENCORE:
1030 Software for Quantitative Ensemble Comparison. *PLoS Computational Biology* **11**, 1–
1031 16 (2015).
- 1032 60. Bottaro, S., Bengtson, T. & Lindorff-Larsen, K. Integrating Molecular Simulation and
1033 Experimental Data: A Bayesian/Maximum Entropy Reweighting Approach. in
1034 *Structural Bioinformatics: Methods and Protocols* (ed. Gáspári, Z.) 219–240 (Springer
1035 US, 2020). doi:10.1007/978-1-0716-0270-6_15.
- 1036 61. Barbet-Massin, E. *et al.* Rapid Proton-Detected NMR Assignment for Proteins with
1037 Fast Magic Angle Spinning. *Journal of the American Chemical Society* **136**, 12489–
1038 12497 (2014).
- 1039 62. Stanek, J. *et al.* NMR Spectroscopic Assignment of Backbone and Side-Chain
1040 Protons in Fully Protonated Proteins: Microcrystals, Sedimented Assemblies, and
1041 Amyloid Fibrils. *Angewandte Chemie International Edition* **55**, 15504–15509 (2016).
- 1042 63. Vranken, W. F. *et al.* The CCPN data model for NMR spectroscopy: Development of a
1043 software pipeline. *Proteins: Structure, Function and Genetics* **59**, 687–696 (2005).
- 1044 64. Schmidt, E. & Güntert, P. A new algorithm for reliable and general NMR resonance
1045 assignment. *Journal of the American Chemical Society* **134**, 12817–12829 (2012).
- 1046 65. Knight, M. J. *et al.* Structure and backbone dynamics of a microcrystalline
1047 metalloprotein by solid-state NMR. *Proceedings of the National Academy of Sciences*
1048 *of the United States of America* **109**, 11095–11100 (2012).
- 1049

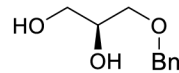




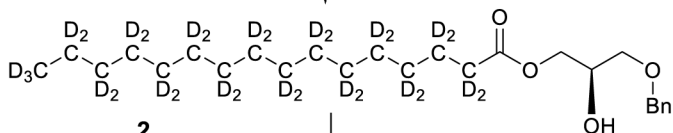




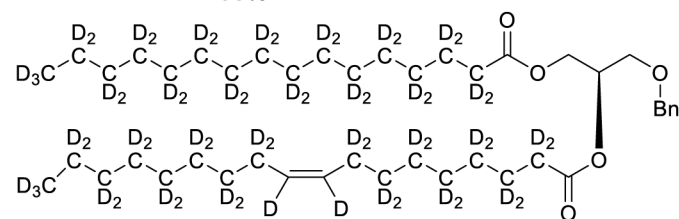




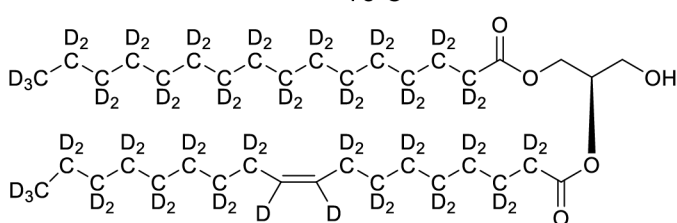
palmitic acid- d_{31} 94%D
 DCC/DCM 80%



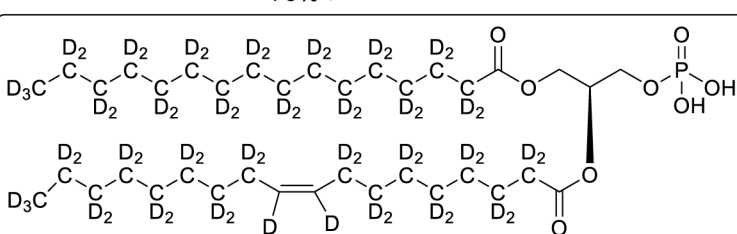
oleic acid- d_{33} 93%D
 DCC/DCM 82%



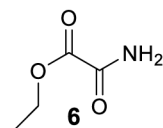
BCl_3/DCM
 -78°C



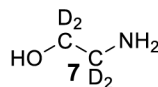
$\text{POCl}_3/\text{Et}_3\text{N}$ toluene
 78%



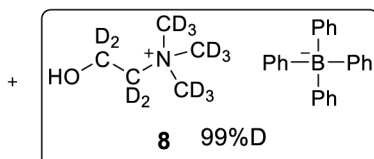
94%D



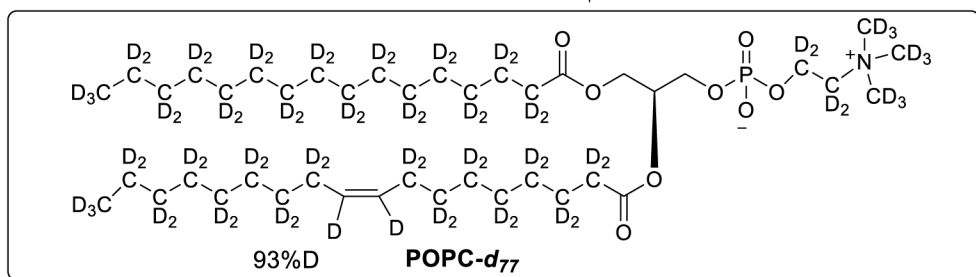
70% LiAlD_4

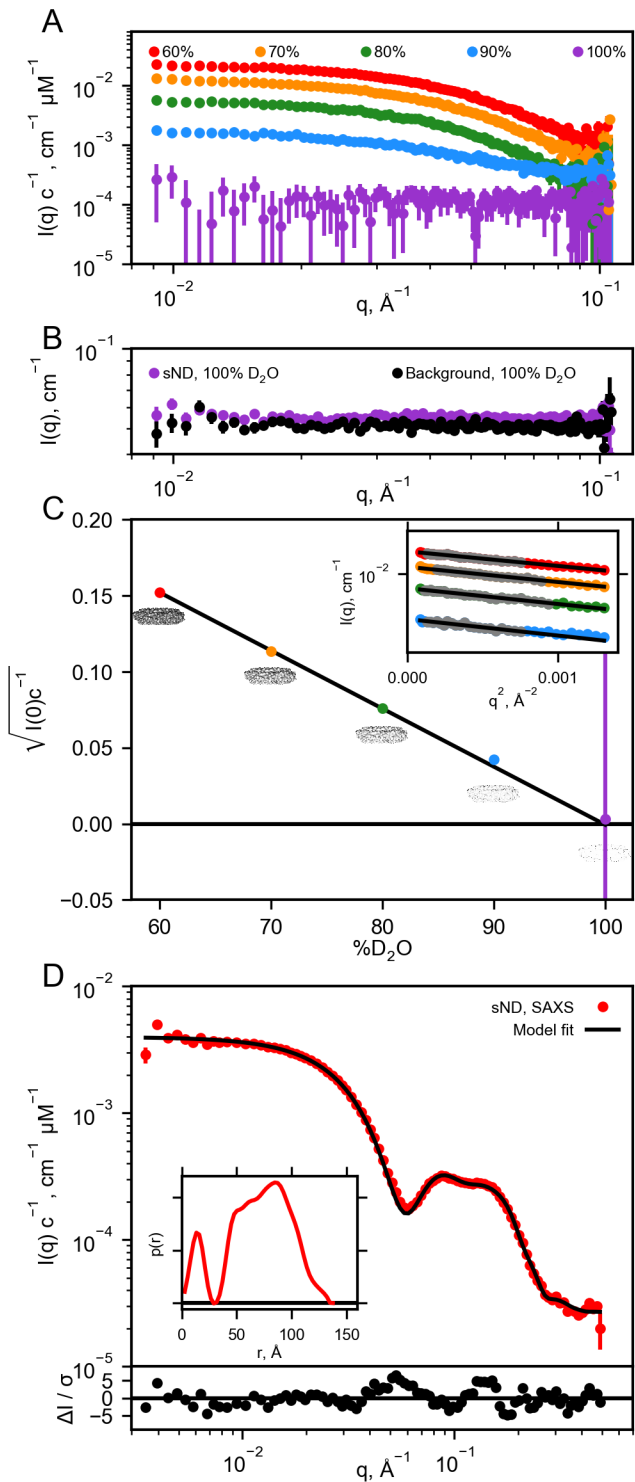


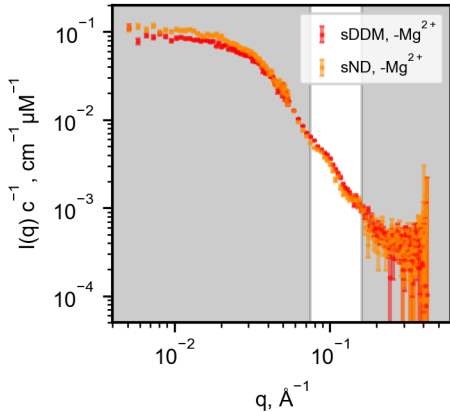
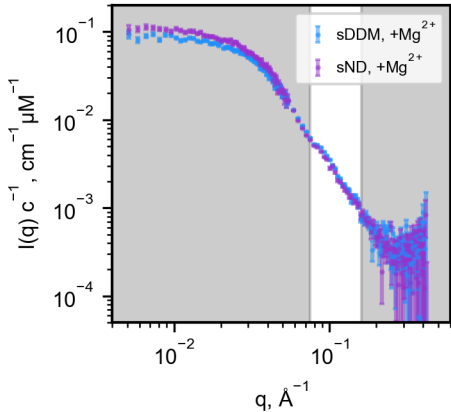
$\text{NaOH}/\text{EtOH}/\text{H}_2\text{O}$ 34%
 CD_3I tetraphenyl borate



39% pyridine/TPS

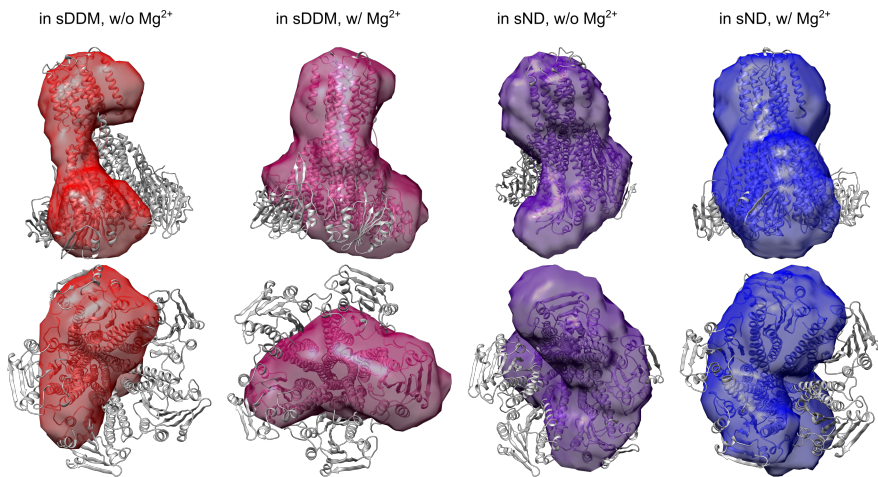




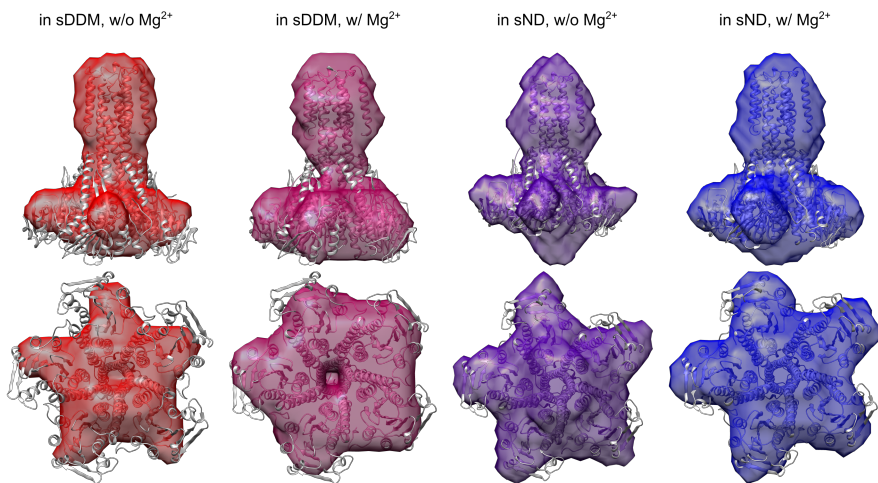


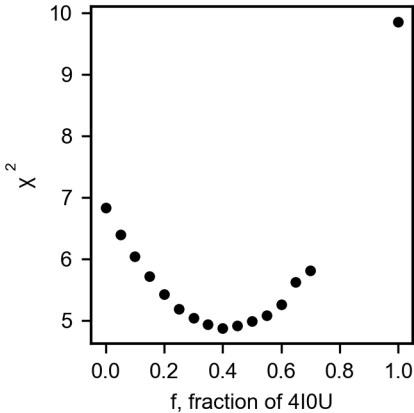
A

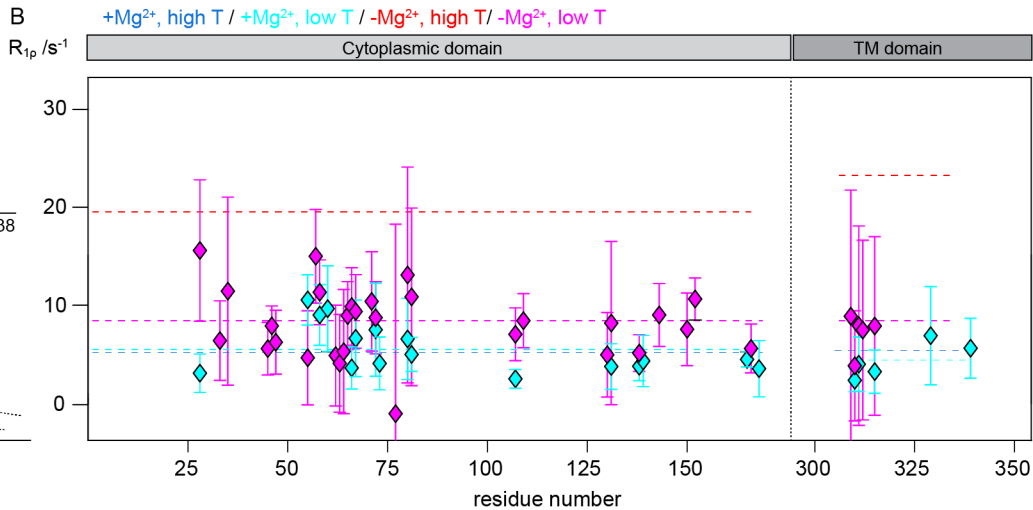
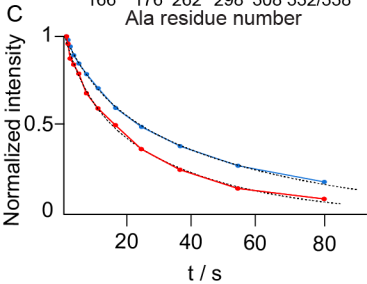
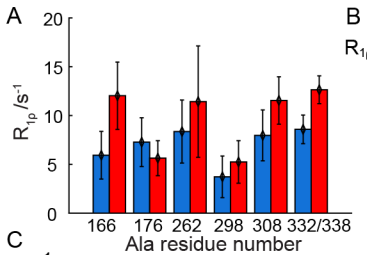
No symmetry (P1) imposed

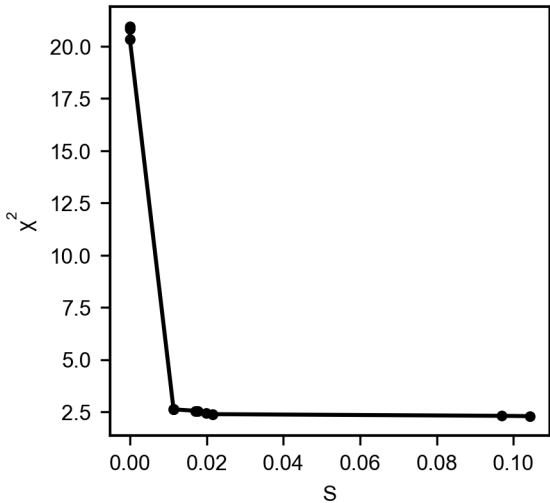
**B**

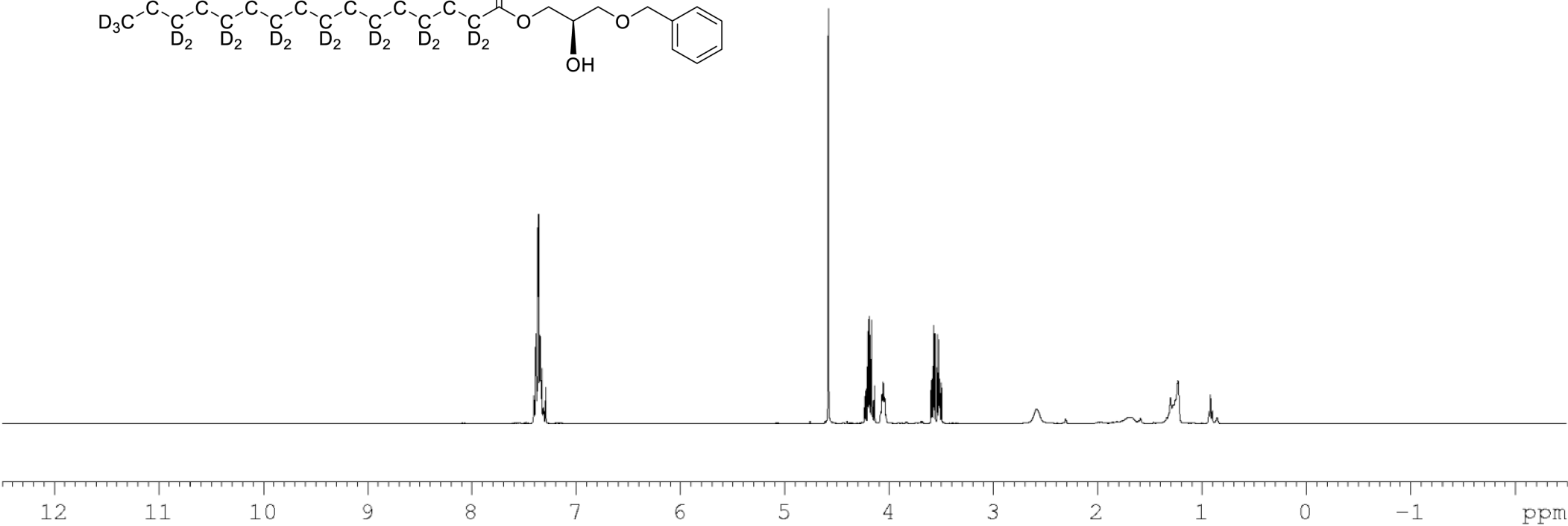
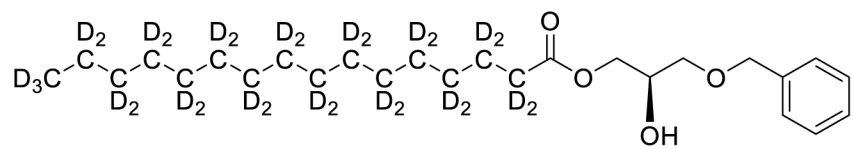
P5 symmetry imposed

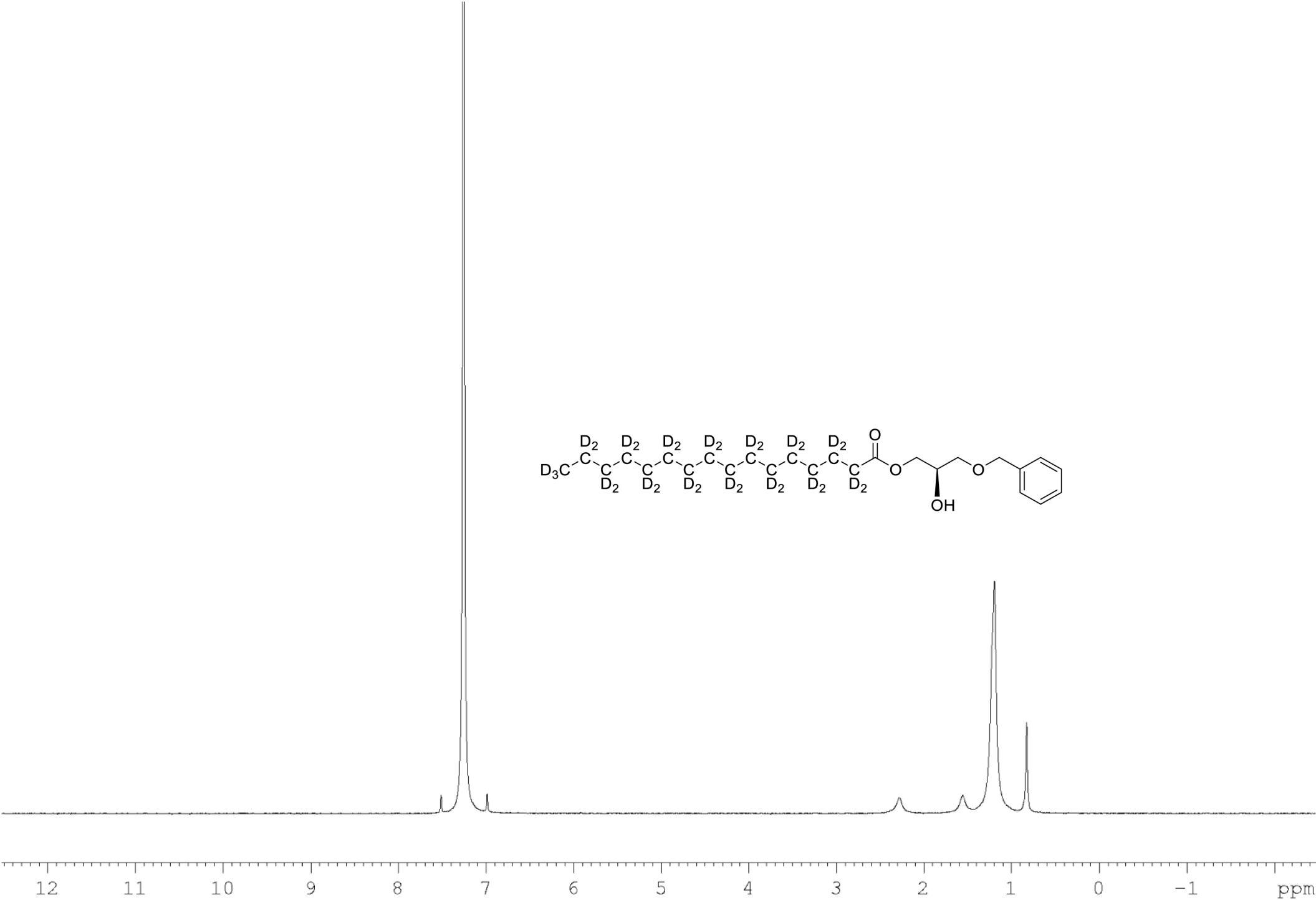


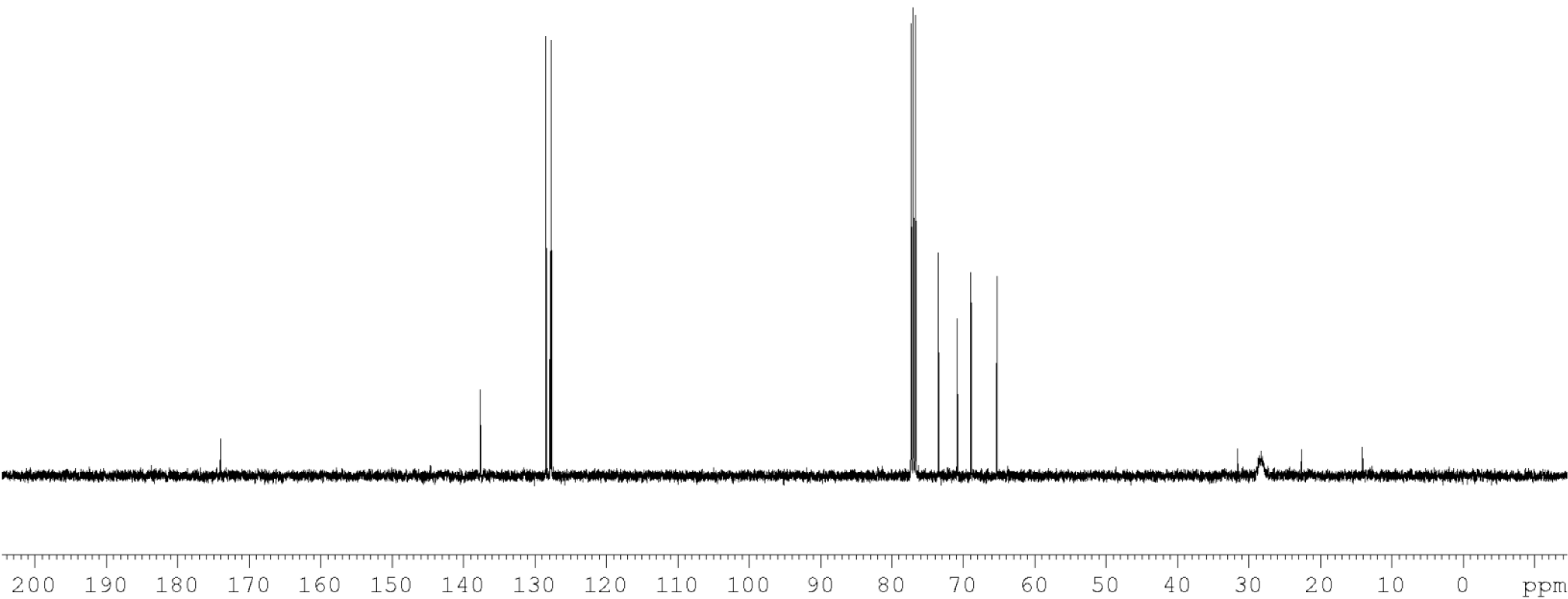
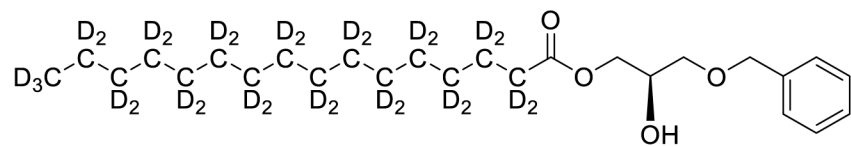


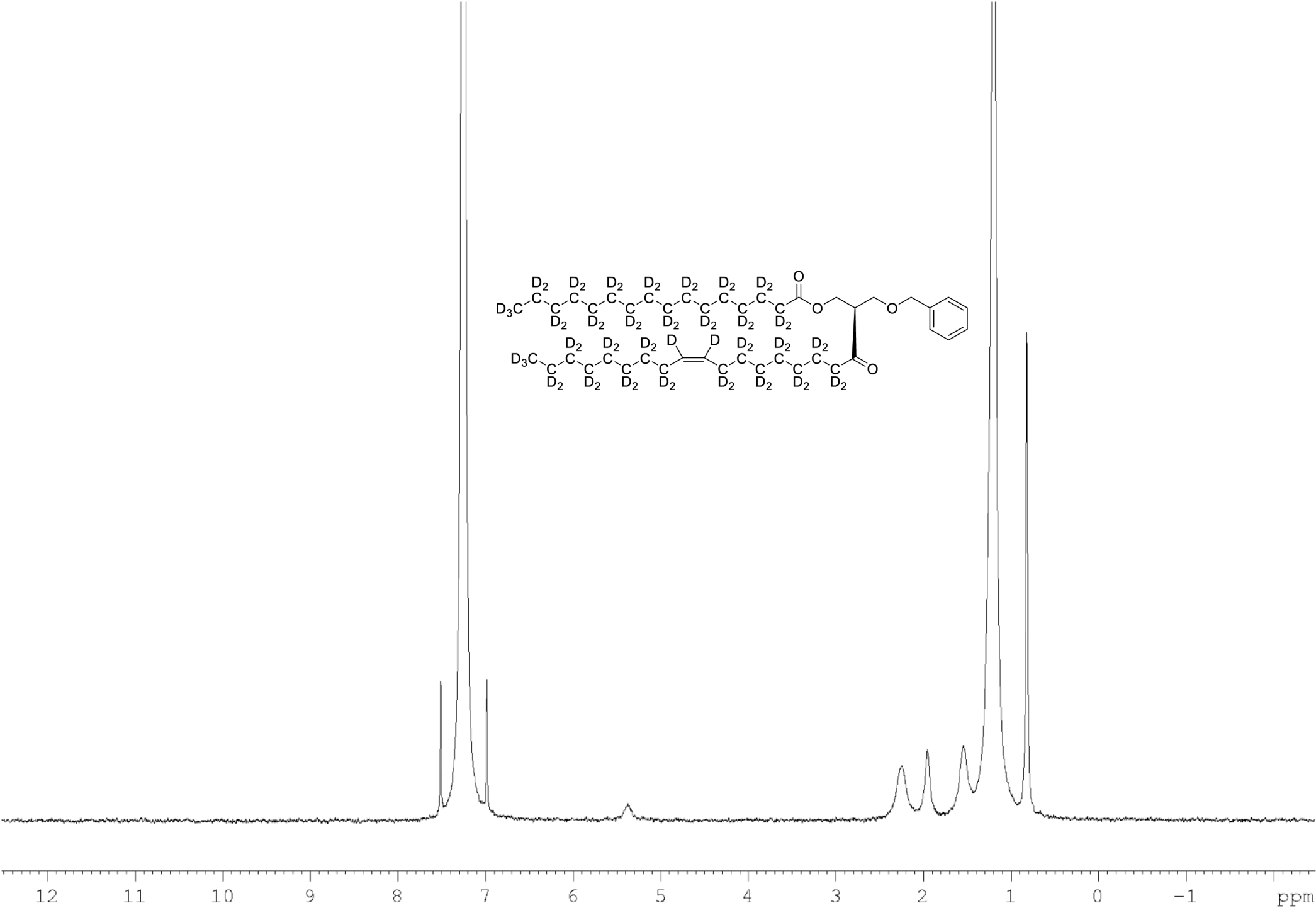


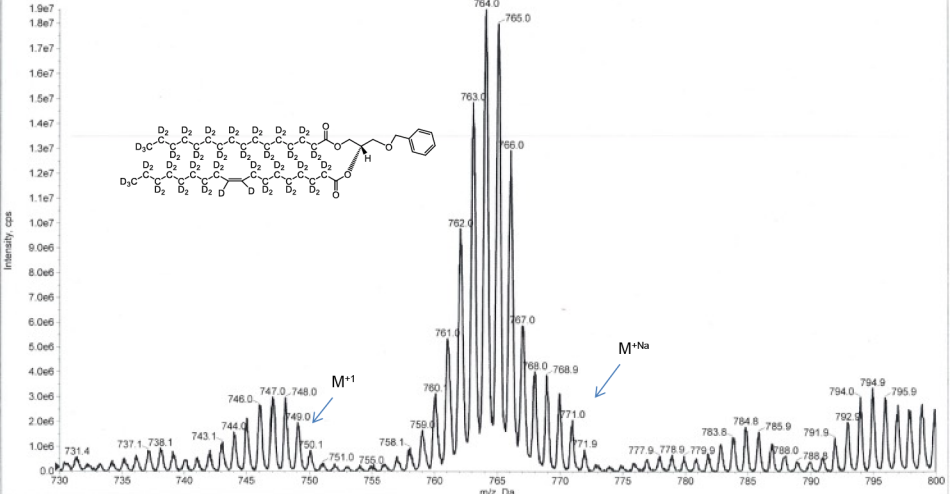
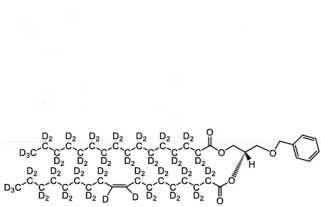


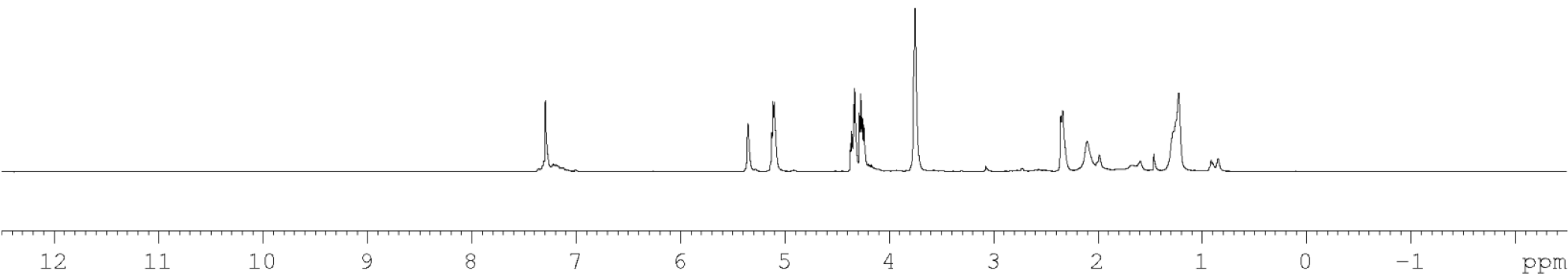
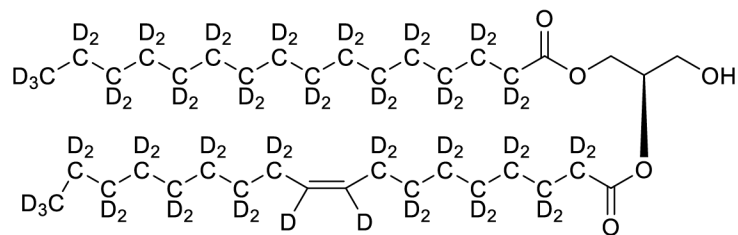


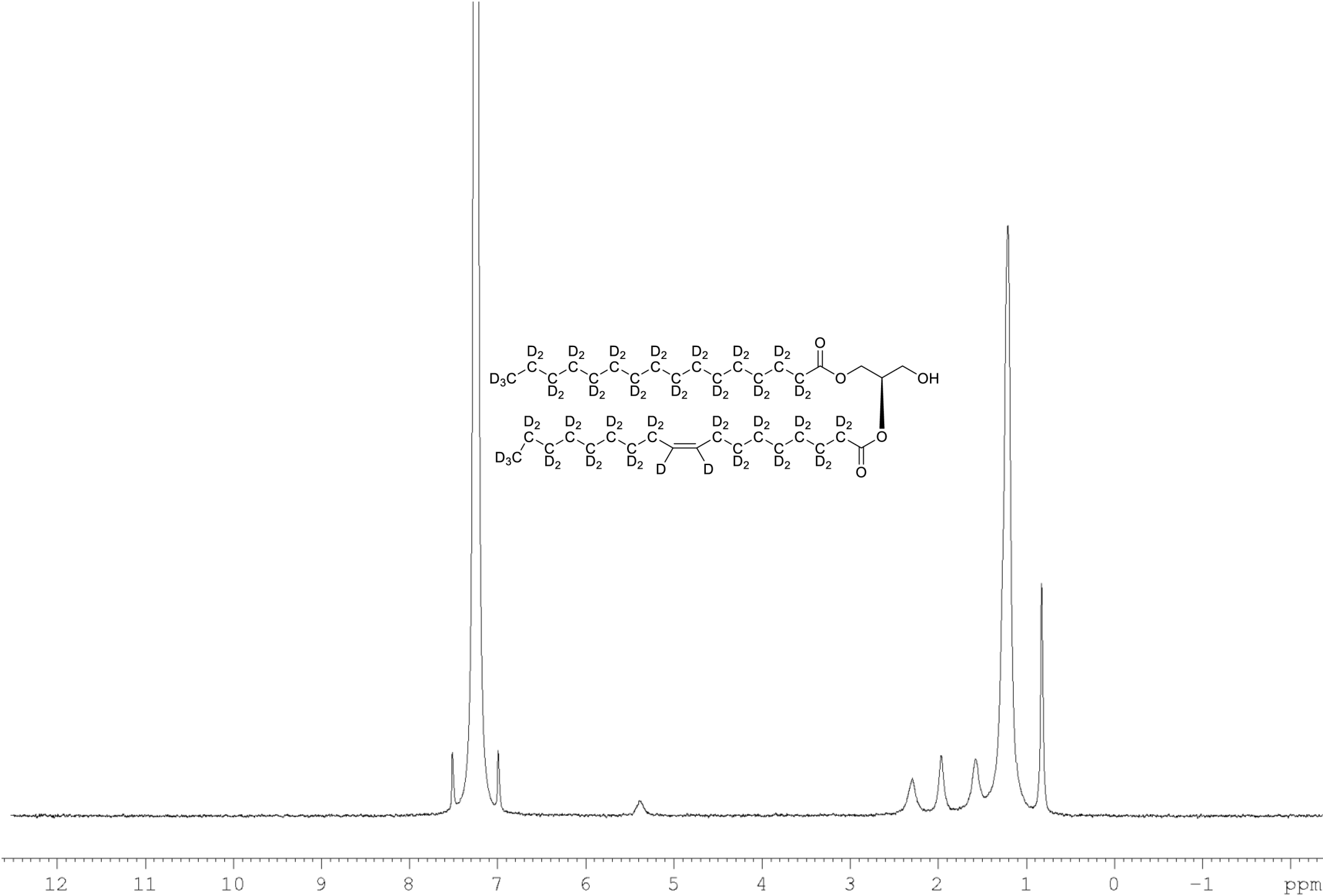


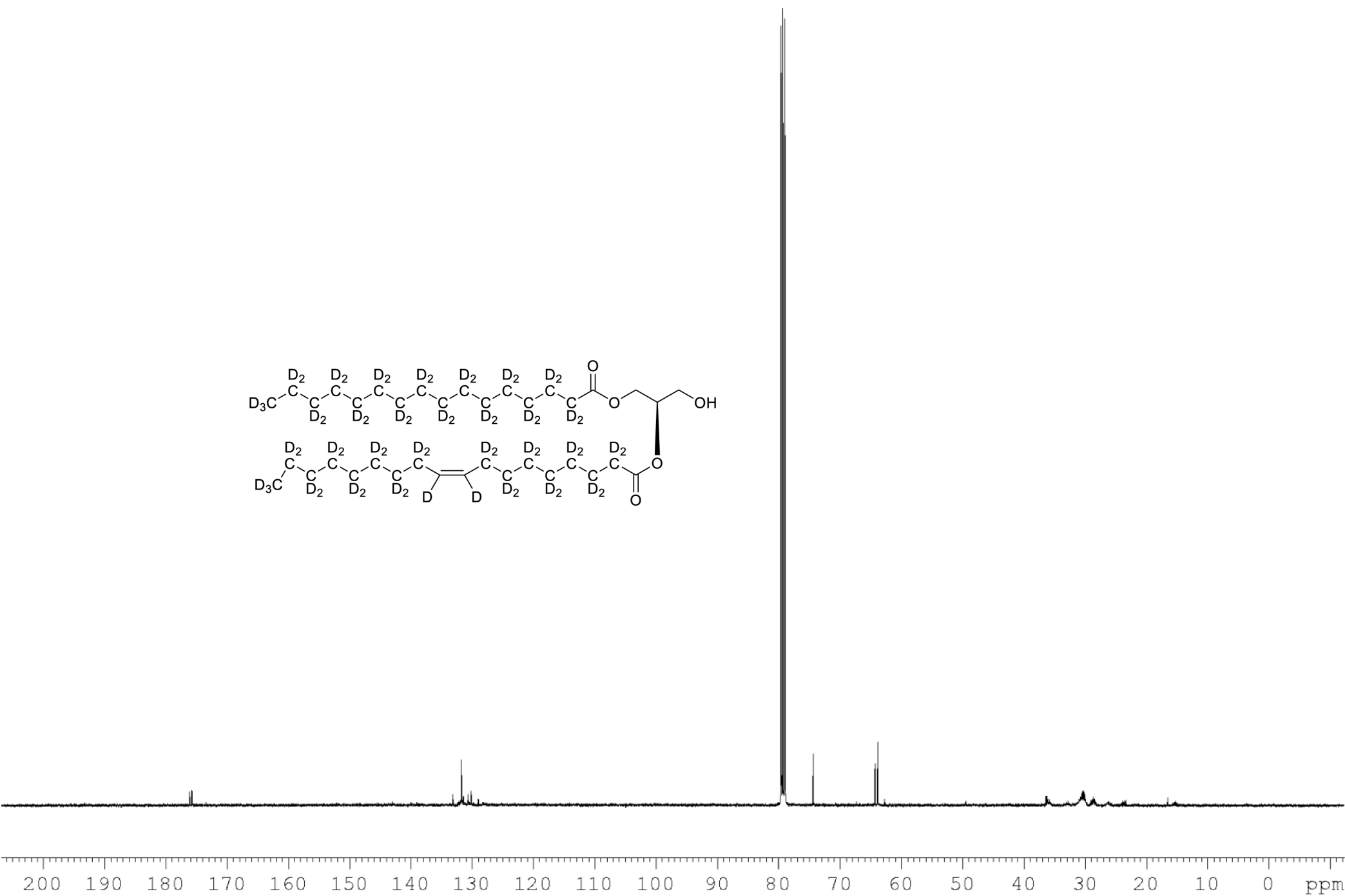
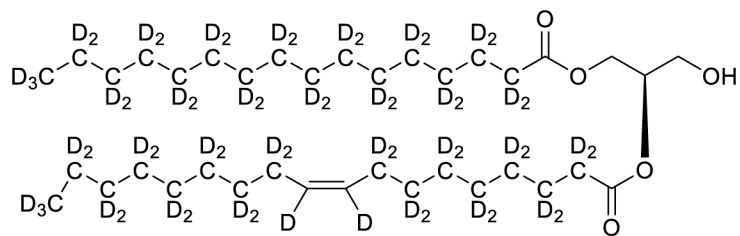


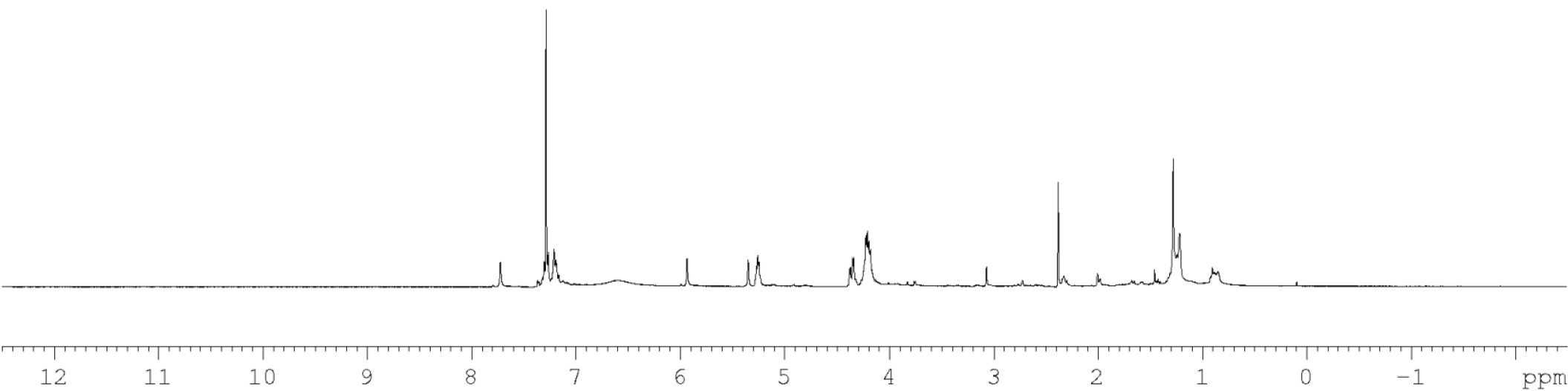
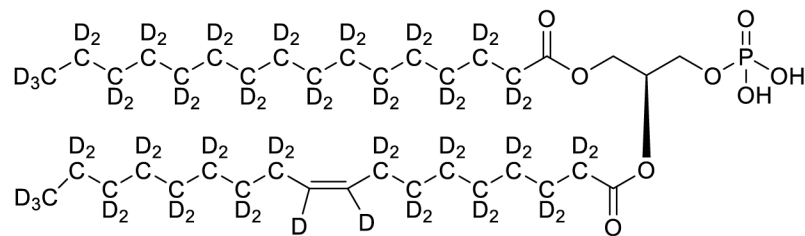


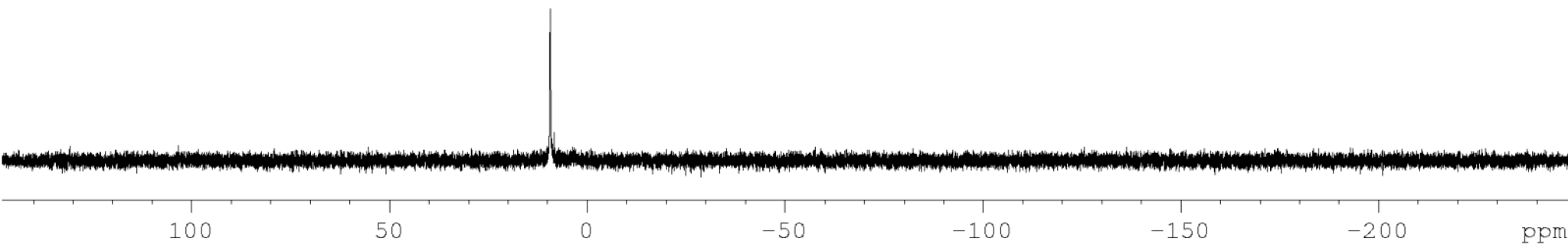
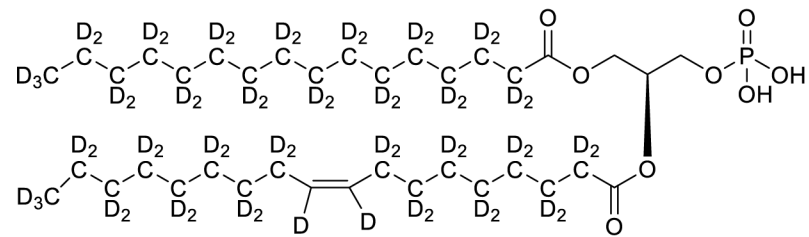


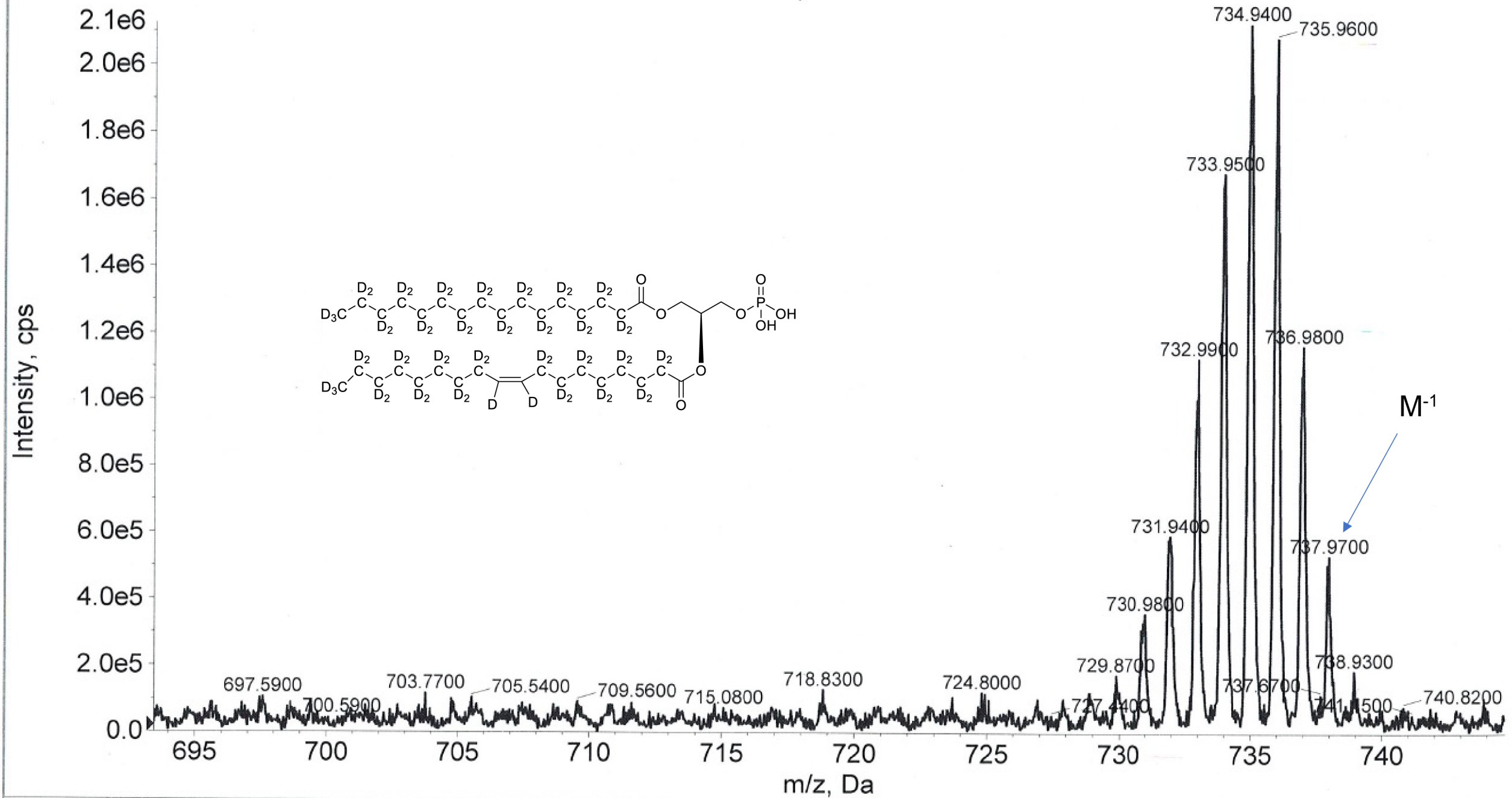


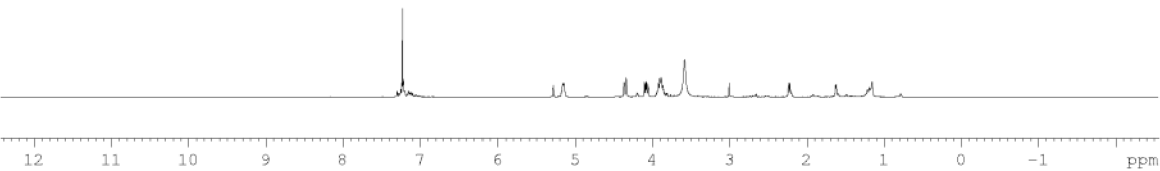
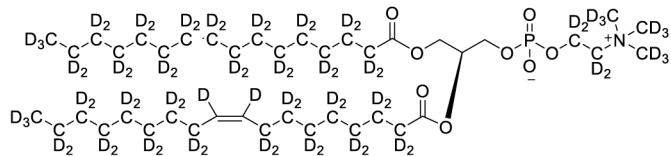


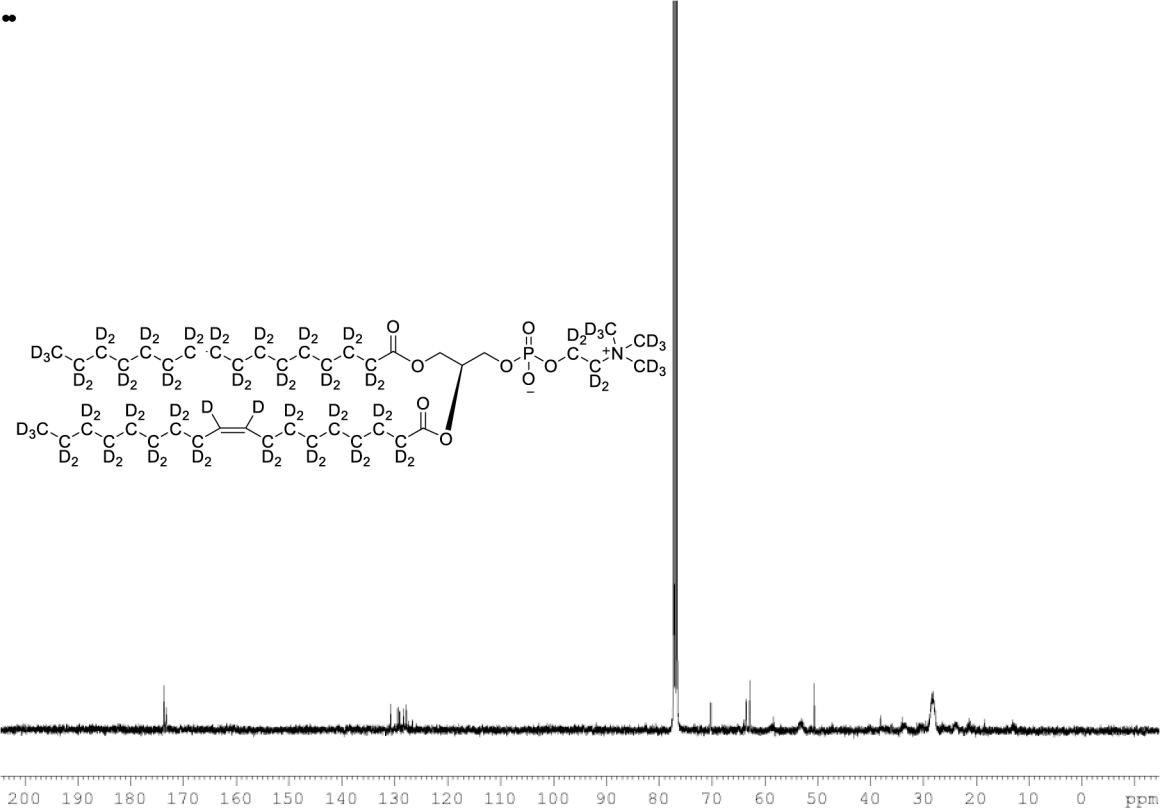
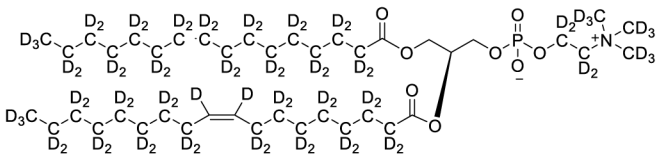


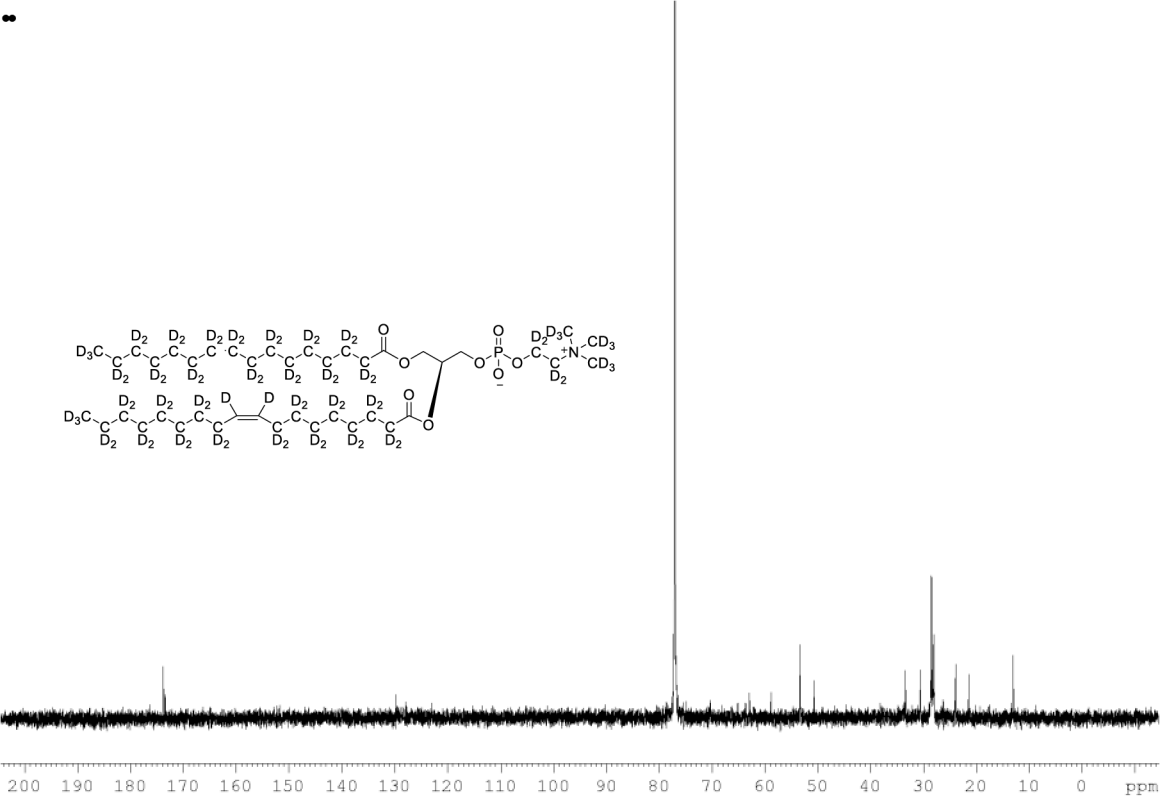
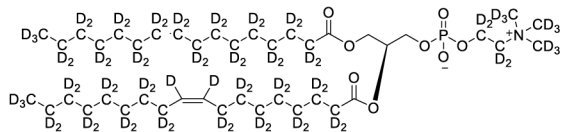




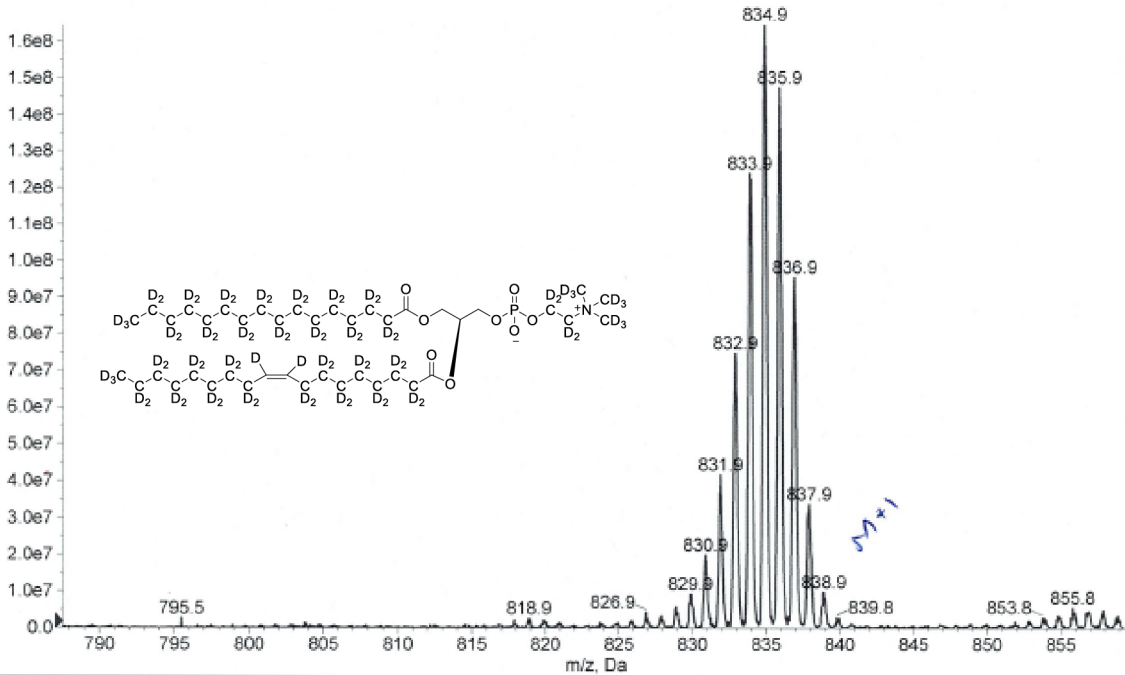


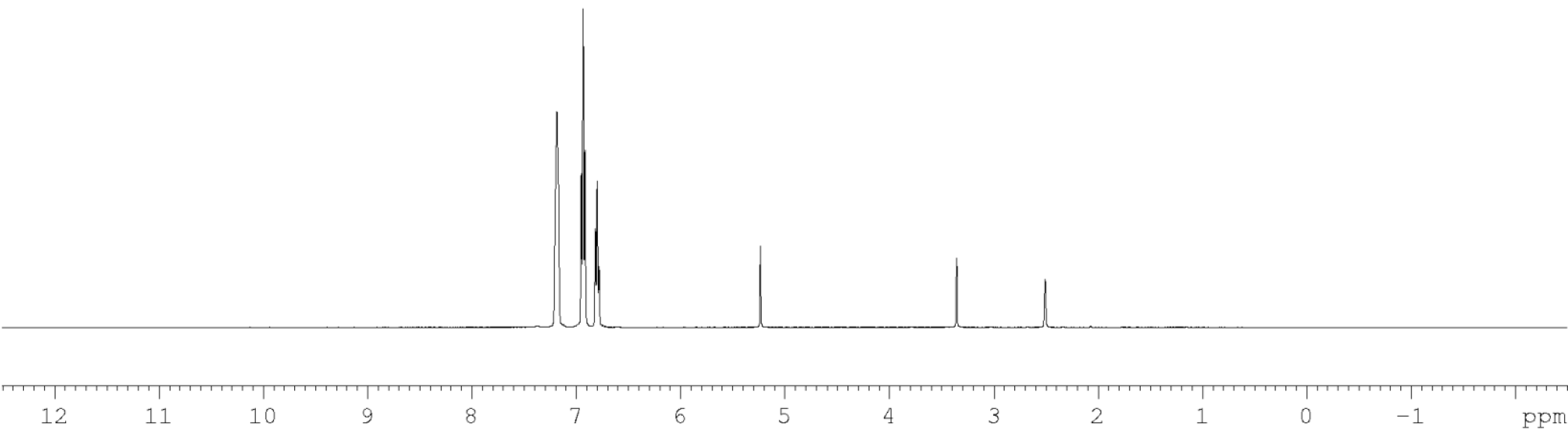
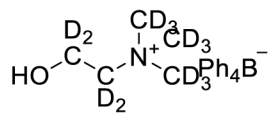


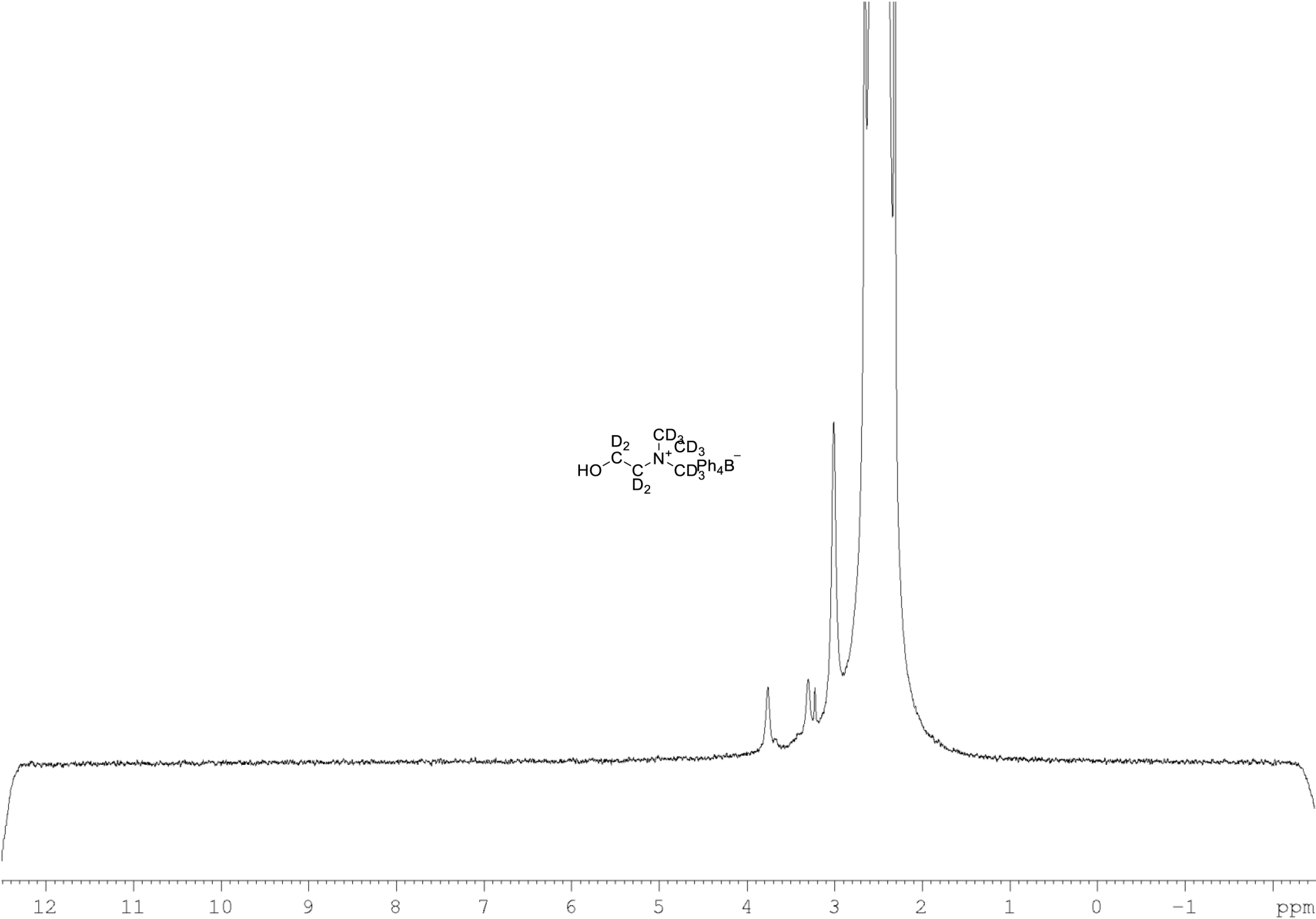


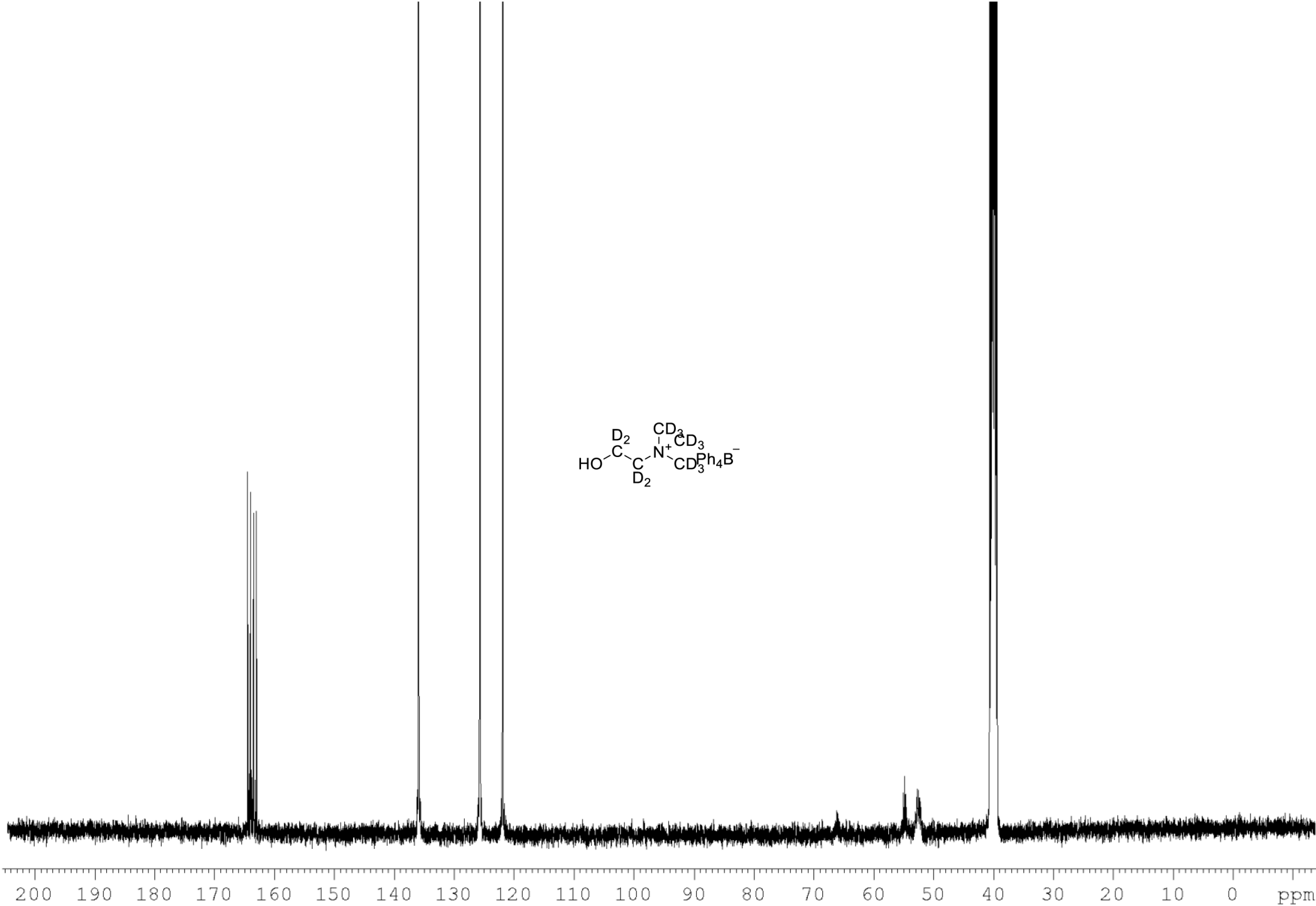


intensity, cps



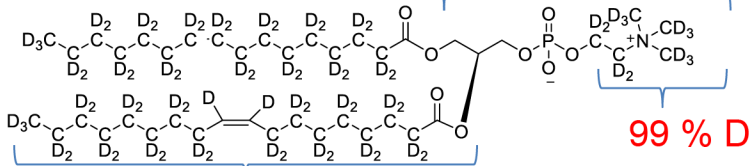






94 % D

71 % D



99 % D

94 % D

93 % D